Numerical simulation of distributed propulsion systems using CFD

Geng Qiao [a], Tao Zhang [b], George N. Barakos [a],*

[a] *CFD Laboratory, School of Engineering, University of Glasgow, Glasgow, G12 8QQ, UK*
[b] *School of Engineering, University of Leicester, Leicester, LE1 7RH, England, UK*

ARTICLE INFO	ABSTRACT
Communicated by Antonio Filippone	This paper examines a Distributed Propulsion (DP) concept and involves CFD verification, optimisation and evaluation. The first part of the study validates the employed simulation methods using experimental data from the NASA Workshop for Integrated Propeller Prediction (WIPP) and the Folding Conformal High Lift Propeller (HLP) project, for isolated and installed cases under various conditions. Additionally, validation for rotor-rotor interactions was also conducted using the GARTEUR Action Group 26 measurements. The second part of the paper examines installed propeller configurations to identify performance differences based on their position relative to a lifting wing. The results indicate that distributed propellers with small radii interfere more with the wing, than tip-mounted, large propellers. Additionally, propeller and wing performance vary with respect to the propeller installation location. The propeller in tractor configuration showed higher efficiency than the over-the-wing (OTW) configuration by about 7%. However, results from this work showed a 2% improvement in the propeller efficiency when the OTW configuration had a pylon installed. This study also found that optimising the propeller from a tractor to OTW configuration, significantly improved the wing performance. At take-off and landing, the Lift-to-Drag (L/D) ratio of the OTW configuration almost quadrupled, and the overall propulsive efficiency increased by about 5%. The simulations showed that the OTW configuration with different numbers of propellers, outperformed the tractor configurations with the same number of propellers. Furthermore, up to 26% improvement in lift and overall propulsive efficiency was found by introducing the DP system in the OTW configuration.

1. Introduction

Aerospace is seeing a growing Urban Air Mobility (UAM) sector, especially in electric vertical take-off and landing (eVTOL) vehicles, due to their zero-emission capabilities and enhanced safety features. Novel vehicle concepts incorporate wing-tip-mounted propellers (WTMP), distributed propulsion (DP) systems, and tandem rotors, resulting in complex flow physics combined by aerodynamic interactions. Consequently, high-precision simulation results and comprehensive experimental databases are indispensable for quantifying and comprehending these complex interactions.

One of the early studies on DP for aircraft propulsion was conducted in 2003 by Andy et al. [1], who assessed the potential advantages of the DP concept. The central idea behind improving the propulsive efficiency involves accelerated air from the trailing edge across part or the entire span of the wing. This study applied analysis to quantify the influence of DP into a Blended-Wing-Body (BWB) Multidisciplinary Optimization Framework. Minimising the takeoff gross weight, and comparing it to a

conventional BWB aircraft, the newly designed aircraft was found to be 4.4% lighter and required 2.7% less fuel. Additionally, the work claims that DP eliminates the need for traditional control surfaces, and offers a reduction in perceived noise.

In a subsequent study in 2010, Kim [2] discussed various DP systems for both subsonic and supersonic vehicle configurations, including the NASA N3-X, Empirical Systems Aerospace ECO-150/250, MIT H3.1, and GIT [3]. These conceptual studies identified several benefits of DP systems, such as reduced fuel consumption by ingesting the wake from propulsors into the airframe wake, achieving high span-wise lift by distributing propulsors, reducing noise through airframe shielding and structural integration, eliminating control surfaces through thrust vectoring, and allowing for high production rates, and easy maintenance of small and lightweight propulsors.

These early conceptual studies on novel propulsion systems suggest that DP systems appear to be an attractive and realistic solution for a wide range of aircraft configurations offering different operational

Nomenclature

C	Tip chord of the rotor blade		AoA	Angle of Attack
C_p	Pressure coefficient, $\frac{p - p_\infty}{0.5\rho U_\infty^2}$		AD	Actuator Disk
C_T	Rotor thrust coefficient, $C_T = \frac{T}{\frac{1}{2}\rho(\Omega R)^2 \pi R^2}$		AP	Auxiliary Propeller
			CCW	Counter Clock Wise
C_{Tprop}	Propeller thrust coefficient, $C_{Tprop} = \frac{T}{\rho n^2 D^4}$		CFD	Computational Fluid Dynamics
			DP	Distributed Propulsion
C_Q	Rotor torque coefficient, $C_Q = \frac{Q}{\frac{1}{2}\rho(\Omega R)^2 \pi R^3}$		HMB	Helicopter Multi-Block
			HLP	High Lift Propeller
C_{Qprop}	Propeller torque coefficient, $C_{Qprop} = \frac{Q}{\rho n^2 D^5}$		GARTEUR	Group for Aeronautical Research and Technology in Europe
c_{ref}	Characteristic length .... m		NASA	National Aeronautics and Space Administration
D	Drag force or Diameter, $D = 2R$ .... N, m		KEAS	Knots Equivalent Air Speed
J	Advance ratio of propellers, $J = \frac{U_\infty}{nD}$		OTW	Over The Wing
k	Turbulent kinetic energy .... $m^2\,s^{-2}$		RB	Resolved Blades
ω	Specific dissipation frequency of turbulence		RPM	Revolutions Per Minute
L	Lift force .... N		RANS	Reynolds-Averaged Navier-Stokes
M_∞	Mach number		SAS	Scale-Adaptive Simulation
n	Rotational speed .... HZ		SST	Shear Stress Tensor
Q	Rotor torque .... N.m		TMS	Time-Marching Simulation
Re	Reynolds number, $\frac{\rho U_{ref} c_{ref}}{\mu}$		TP	Tip-mounted Propeller
			URANS	Unsteady Reynolds-Averaged Navier-Stokes
R	Radius .... m		WIPP	Workshop for Integrated Propeller Prediction
R	Flow residual vector			
T	Rotor thrust .... N			
U	Local velocity .... m/s		*Greek*	
U_∞	Free-stream velocity .... m/s		η	Froude efficiency, $\eta = \frac{TU_\infty}{Q\Omega}$
W	Flow variable vector		ρ	Density .... kg/m³
Acronyms			μ	Advance ratio of rotors, $\mu = \frac{U_\infty}{\Omega R}$

possibilities, while addressing environmental and energy concerns in the context of the growing demands of aviation.

In recent years, several distributed electric propulsion designs have been proposed. For instance, the NASA X-57 Maxwell aircraft, developed by ESAero, incorporates 12 small electrically-driven propellers distributed along the wing in front of the leading edge, along with 2 large propellers mounted at the wing-tips [4] [5]. XV-24 utilises multiple electric fans not only for VTOL capability but also for achieving high cruise speeds [6]. With the emergence of the "air-taxi" market, and the potential advantages of DP systems, various VTOL aircraft concepts have been proposed and developed by companies like Joby Aviation in California, US (S2 aircraft), Lilium jet in Munich, Germany, and Vertical Aerospace in Bristol, UK (VX4). Most recently, the S2 aircraft of Joby Aviation has been delivered to the U.S. Air Force and is currently undergoing assessments.

In this context of research, Reynard et al. [7] proposed a preliminary sizing method for hybrid-electric DP aircraft. Their work takes into account the powertrain architecture, and the associated effects of integrating propulsion systems with the airframe, making it suitable for the conceptual design process of hybrid-electric aircraft. By comparing three powertrain architectures, it was observed that while the energy consumption increased by 3% when implementing the DP system, there was a significant increase in wing loading, and 6% improvement in lift-to-drag ratio at cruise.

Furthermore, in 2014, Müller et al. [8] discovered that the use of high-speed propellers, in combination with internally blown flaps, can enhance the performance of cruise-efficient, short take-off and landing (STOL) aircraft. Building on these findings, their study compared various propulsion systems, including clean, tractor, OTW, and channel wing configurations, utilising a steady-state actuator disk model. The results indicated that the OTW configuration appears promising for integrating into DP systems.

Marcus [9] investigated OTW propellers for DP systems, employing a combination of experiments and low-fidelity numerical tools. The low-fidelity numerical tools encompassed non-uniform inflow, and blade-element model for the propeller, a panel method for the wing, and a vortex lattice model for the propeller slipstream. After validating this low-fidelity numerical tool using wind tunnel data, the effects of the axial position and diameter of the propeller were assessed. The results revealed that the optimal axial propeller position is near the trailing edge of the wing. In this location, the lift produced by the wing was increased by 8% and 3% in cruise, and high-lift configurations, respectively. Additionally, reducing the propeller diameter while maintaining a constant thrust coefficient at this location yielded performance benefits.

In 2021, Reynard et al. [10] conducted a comprehensive wind tunnel investigation into the OTW propeller boundary layer interaction. Their experiments, involved placing the OTW propeller above the hinge line of the wing. Measurements were taken with and without axial pressure gradients, encompassing both time-averaged, and unsteady interactional effects. Their work also revealed that positioning the propeller over the wing surface induced an adverse pressure gradient on the wing, which was linearly proportional to the thrust. Consequently, increasing the blade-tip clearance resulted in a reduction in thrust. The authors attributed this to the contraction of the slipstream, leading to a deceleration of the flow near the surface of the wing. Additionally, the presence of the propeller blades induced fluctuations in the surface pressure, and contributed to an increase in time-averaged pressure due to flow deceleration. Furthermore, the study explored different propeller locations and observed that increasing the tip clearance did not effectively alleviate flow separation. Conversely, positioning the propeller half a radius upstream of the hinge line generated a Coanda effect, which caused the flow to attach to the flap surface due to suction. This effect, in turn, led to a noticeable increase in lift for the entire configuration.

In the same year, Reynard et al. [11] studied aerodynamic interactions in distributed propellers at forward flight. Their experimental results showed that in a three-propeller configuration, there was 1.5% decrease in performance observed from the middle propeller. This penalty was found to be insensitive to the rotation direction and relative blade phase angle. Additionally, the slipstream from adjacent propellers, induced local loading variations on the propeller disk, ranging from 5% to 10% of the average disk loading. Noise measurements indicated that interactions in distributed propellers altered the tonal noise waveforms compared to the case with a single propeller installed. Furthermore, the study explored an active control method by changing the relative blade phase angles between propellers, to effectively modify the noise directivity pattern of the DP system.

In 2023, Reynard et al. [12] expanded the OTW DP system from component to aircraft level to assess its continued applicability. Preliminary sizing was conducted based on a partial-turboelectric regional passenger aircraft and its performance was compared with that of a conventional twin-turboprop aircraft. Experimental data was used to validate a low-order method used for the investigation of un-ducted OTW DP system. At cruise, for an aircraft with 53% of its wingspan covered by the OTW DP system, the numerical method demonstrated a 45% improvement in local lift-to-drag ratio at cost of 12% reduction in propeller efficiency. The aerodynamic coupling was found to increase the propulsive efficiency of the aircraft by 9% over a 1500 nautical mile mission. Additionally, this work considered the increase in takeoff mass due to the electrical drivetrain and a reduction in fuel weight achieved by implementing the OTWDP system, resulting in a 5% reduction in overall energy consumption.

Previous investigations transitioned from conventional tractor propulsion systems to over-the-wing distributed propulsion (OTWDP) systems, gradually increasing the fidelity from low-order models, steady-state actuator disk simulations, and experimental methods. However, it is rare to find studies examining both conventional and OTW propulsion systems, with equivalent performance at high load conditions. The benefits of the OTW configuration and OTWDP system, when directly compared to equivalent conventional tractor configurations, remain unexplored and not quantified. Furthermore, the impact of the pylon structure in the OTW configuration has been overlooked in previous studies, both with low-order simulations and experiments. The pylon structure not only creates a blockage effect for the propeller but also adds more surface area, increasing drag on the entire propulsion system. Additionally, neither configuration, when integrated with a distributed propulsion system, has been fairly compared or thoroughly investigated using either experiments or fully resolved simulations. As a result, future distributed propulsion designs may lack certainty regarding which configurations to adopt. To address these critical gaps in the research, this paper aims to provide comprehensive insights and quantitative assessments of tractor and OTW DP systems at high performance condition.

2. Numerical methods

2.1. HMB3 CFD solver

The in-house Helicopter Multi-Block (HMB3) CFD solver is employed in this study. HMB3 can predict the aerodynamic performance, and acoustics of propulsion systems, as shown in previous studies [13] [14]. HMB3 has been widely used in the investigation of rotorcraft flows [15] [16] [17] [18], helicopter rotor aeroelasticity [19], propeller aeroacoustics [20], flight mechanics [21] and missile trajectory prediction [22]. Moreover, good agreement when compared to experimental results in aerodynamics, acoustics and aeroelasticity of propellers, has been reported in previous studies [23–26]. Most recently, its ability to capture the interactions of multi-rotor flows, and the performance of ducted propellers was also documented [27–30].

HMB3 solves the Unsteady Reynolds Averaged Navier-Stokes (URANS) equation in integral form using the Arbitrary Lagrangian-Eulerian formulation for time-dependent domains, including moving boundaries. HMB3 uses a cell-centred finite volume approach to discretise the Navier-Stokes equations on multi-block, structured grids.

$$\frac{d}{dt}\left(\mathbf{W}_{i,j,k} V_{i,j,k}\right) = -\mathbf{R}_{i,j,k}\left(\mathbf{W}_{i,j,k}\right), \tag{1}$$

In Equation (1), i, j, k represent the cell index, $\mathbf{W}$ and $\mathbf{R}$ are the vector of conservative flow variables and the residual respectively, and $V_{i,j,k}$ is the volume of the cell i, j, k. The convective fluxes are evaluated using Osher's approximate Riemann solver, while the viscous terms are discretised using a second-order central differences scheme. The third-order MUSCL (Monotone Upstream-centred Schemes for Conservation Laws) approach provides high-order accuracy in space. In the present work, simulations are conducted using the $k-\omega$ shear stress transport (SST) turbulence model [31] as this has been well-validated in previous studies of interactional aerodynamics [32,33].

For isolated rotors and propellers in axial flight, the azimuthal symmetry of the configuration can be exploited, whereby only a fraction of the grid needs to be generated. The Rotating Reference Frame (RRF) method is implemented in HMB3 [34] for simulations with rotational periodicity. The governing flow equations are reformulated and solved in a non-inertial reference frame, thus transforming the unsteady problem into a steady one. The Froude condition is using a potential-sink for the inflow and outflow instead of freestream values. This has been extensively validated and used in previous works [29,35]. The advantage of this method is that it uses the rotor thrust to compute the strength of the potential sink placed at the rotor origin, hence accelerating the convergence of the simulation.

For unsteady simulations, the entire grid is required. However, this can be obtained by copying and rotating the grids of the steady simulations using the HMB3 tools. Additionally, unsteady calculations are possible, using the implicit, dual-time stepping approach. The computational grids used for rotors, pylon and lifting surfaces have a typical C-H topology. The spacing distribution has been set to the condition $y^+ \leq 1$ [36], resulting in a first cell size normal to the surfaces of approximately 2.0×10^{-6}m $(1.0 \times 10^{-5} c_{ref})$ as tested a-posteriori. Adiabatic, non-slip, wall boundary conditions were applied at rotors, lifting surfaces, pylon and nacelle, with freestream values applied at far-field boundaries.

Chimera overset grids have been employed to capture the high-pressure gradient region, and have been carefully designed for efficient load balancing. The Chimera moving mesh approach involves pre-processing to determine the potential overlap between blocks, overset mesh search to localise cell-to-cell overlapping using a tree structure for efficiency, and interpolation weight calculation for the cells that require interpolated data. The interpolation is crucial for maintaining accuracy, as the halo cells of the mesh must be correctly populated. To this end, this work applied second-order flow variable distribution, with a reconstruction-based interpolation built into the HMB3 tool. The overset mesh method of HMB3 and its applications in wing, rotor, and rotor fuselage configurations have been demonstrated in [37].

For unsteady computations, a time step corresponding to one degree of propeller rotation, was used for all cases. The convergence of the implicit scheme was determined based on the reduction of the flow field residual, compared to the previous time step. In particular, either a three-order-of-magnitude reduction or 300 inner iterations, was considered sufficient for each unsteady step.

Furthermore, to assess the interference between propellers and lifting surfaces, it is evident that both components of each configuration cannot be independently evaluated. Thus, an integration of relevant forces (Thrust T, drag D) should be employed to comprehensively compare the overall performance of different configurations.

In Equation (2), the overall installed thrust ($T_{install}$) is calculated by subtracting the drag ($D_{lifting\ surface}$) of the lifting surface from the total thrust ($T_{propellers}$) generated by the propellers.

(a) Rotor disk and local forces in a space cylindrical coordinate system.

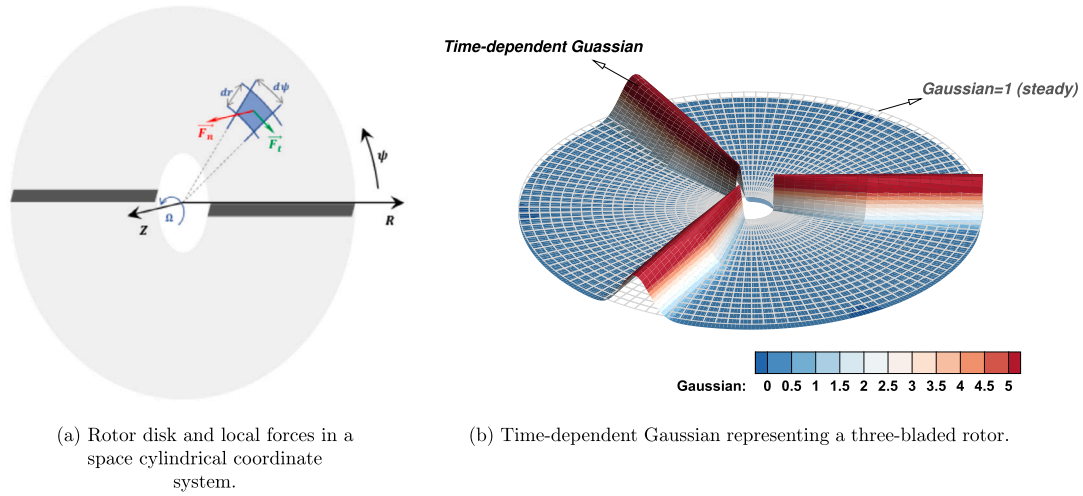(b) Time-dependent Gaussian representing a three-bladed rotor.

Fig. 1. Illustration of the actuator disk modelling of rotors. (For interpretation of the colours in the figure(s), the reader is referred to the web version of this article.)

$$T_{install} = T_{propellers} - D_{lifting\ surface} \qquad (2)$$

Subsequently, the overall propulsive efficiency can be simplified, This can be seen in Equation (3). Here, V_∞ represents the free-stream velocity, and P_{shaft} denotes the power required by the propellers.

$$Overall\ propulsive\ efficiency\ (\eta) = \frac{T_{install} \times V_\infty}{P_{shaft}} \qquad (3)$$

Finally, this study will apply the aforementioned equations to evaluate the overall performance of equivalent tractor and OTW distributed propulsion systems, where ensuring that the lifting surface is trimmed to produce the same amount of lift.

2.2. Actuator disk/line models

The current study used the actuator disk representation of rotors for modelling interactional aerodynamics. The actuator disk is an efficient modelling approach offering reduced computational cost but has low fidelity. It has been widely used for rotors [38,39] and propellers [40]. Here, the actuator disk model is implemented as equivalent momentum and energy sources injected into the flow field, with an illustration of the method presented in Fig. 1.

Dividing a rotor disk into segments, in a polar coordinate system, centred at the rotor hub, as shown in Fig. 1(a), the local force vector for a specific cell is correlated with a pressure jump using:

$$T = a_x \int_0^{2\pi} \int_{R_{rt}}^{R_{tp}} \Delta P(r,\psi)g(r,\psi,t)\sigma(x,y,z)drd\psi, \qquad (4)$$

$$Q = a_t \int_0^{2\pi} \int_{R_{rt}}^{R_{tp}} \Delta P_t(r,\psi)g(r,\psi,t)\sigma(x,y,z)r^2 drd\psi, \qquad (5)$$

where (r,ψ) are the local polar coordinates on the disk, with the subscripts rt, tp denoting the root and tip values, respectively. Here, a_x and a_t are scaling factors ensuring that the total thrust or torque imposed to the flow-field equals to specified amounts, and $\sigma(x,y,z)$ is a distribution function introduced to adjust the strength of the disk in space. $\Delta P(r,\psi)$ is the pressure jump distribution function that depends on the rotor aerodynamic characteristics. In the present work, we used a uniform disk model for the axial flight propeller. The function $g(r,\psi,t)$ is a time-dependent Gaussian to redistribute the initial pressure jump in space to resemble discrete blades [41], as shown in Fig. 1(b).

2.3. Kriging surrogate model

The Kriging surrogate model [42] is an interpolation method based on Gaussian regression, and is used here to search for optimal configurations of propellers. Kriging, estimates the value of an unobserved evaluation point using a predictor function plus a small, stochastic variance as follows:

$$Z(\mathbf{x}) = Z_0 + \epsilon(\mathbf{x}), \qquad (6)$$

where $Z(\mathbf{x})$ is the prediction at the unknown location $\mathbf{x}$, and Z_0 is the mean value of the data set. $\epsilon(\mathbf{x})$ is a random variable depending on the distance between the unknown point, and the sampling points, and has a mean value of zero. In most cases, it is common that values at the interpolation points are very similar to their immediate known neighbours, and have weaker correlations with sampling points that are far away. The Kriging model uses prescribed variograms to describe the correlation between the sampling and predicted points, thereby solving for the term $\epsilon(\mathbf{x})$ for the interpolation [42]. Kriging models can be categorised into different types, depending on the function types of Z_0 and $\epsilon(\mathbf{x})$ used. The current work adopts the Ordinary Kriging with Z_0 denoted by a constant, and $\epsilon(\mathbf{x})$ is a normal distribution [42]. More details can be found in the work by Saves et al.[43].

Compared to deterministic interpolation methods e.g. radial-base functions or polynomial approximations, the benefit of Kriging is that it provides not only predictions of function values at unobserved points, but also the uncertainty of the predictions. Kriging has hence been widely used in various applications, including aerodynamic shape optimisation studies. The drawbacks are the slightly larger computational cost for solving linear systems (which scales with the number of sampling points) and a few assumptions on the data set, in terms of stationarity and compliance with normal distributions. Nonetheless, these disadvantages are not critical, as the demanded computational cost is much smaller than the CFD simulations, and the assumptions can be examined by verifying and assessing the interpolation results.

3. CFD validation

This study aims to evaluate distributed propellers with various configurations using both reduced-order, and high-fidelity methods, and demonstrate the different interactions that occur with various designs and how they affect performance. Therefore, it is crucial to ensure that the geometries, grids, and methods used in this work are capable to accurately capture the performance and complex flow phenomena. To this end, this section presents validation using data from three sources. The validation includes data from the WIPP [44], conformal High-Lift Pro-
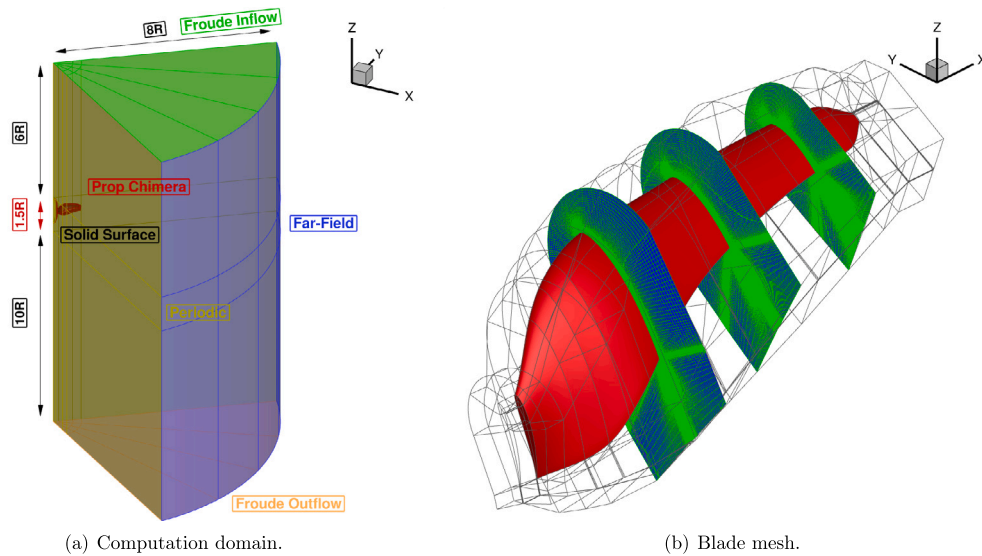
(a) Computation domain.

(b) Blade mesh.

Fig. 2. Conformal HLP mesh details.

peller (HLP) experiments [45], and investigations of multi-rotor systems from the GARTEUR Action Group 26 (AG26) project [46].

3.1. Isolated folding conformal high lift propeller

In a DP system, it is possible to use smaller propellers compared to those used in a tip-mounted configuration [47]. Litherland et al. [45] conducted wind tunnel tests on a conformal high-lift propeller (HLP), which was designed for use with the DP system of the X-57 "Maxwell" electric aircraft. The X-57 utilises twelve fixed-pitch, conformal, high-lift propellers mounted on the wing leading edge to increase lift at low speeds. The conformal design enables the blades to fold into the nacelles at cruise, reducing drag and performance losses. The experiments involved measuring the performance of conformal high-lift propellers at various advance ratios and compared it with low and high order prediction models [44] [48].

This section presents the validation of the conformal/non-conformal HLP. The HLP has five blades with a radius of 0.288 m, and a pitch angle of 24.1 degrees at 75% of the blade radius. Advance ratios J from 0.65 to 1.17 were tested with varying RPMs from 4200 to 4800, and flight velocities from 30 m/s to 54 m/s. The blade was of a constant MH114 aerofoil profile, which was modified to include a 5.08×10^{-4} m (0.02 inch) thick trailing edge for easier manufacturing. The modification was achieved by relofting the blade upper surface and rotating it back to prevent changes in the aerofoil chord line. The non-conformal propeller blades were given rake and skew parameters to become foldable without performance loss.

The blade geometry was then generated using OpenVSP [49] of NASA using twist, chord, skew and rake distribution, and its details can be obtained from [45]. In addition to the blade design function, OpenVSP also provides aerodynamic analyses using low-order methods, including actuator disk models, and vortex lattice methods. In this work, the OpenVSP results [45] were used as part of the CFD mesh generation.

The $1/N_b$ computational domains presented in Fig. 2 were used for the validation of the folding conformal HLP. The computational resources were reduced due to the rotating reference frame, and the periodic domain. Froude conditions were also used by defining a thrust coefficient, and a source-sink model was placed in the centre of the rotor to accelerate the convergence of simulations.

After preparing the propeller geometry and the CFD grids, the test condition were used defined by Litherland et al. [45] and are shown in Table 1. High performance condition was selected and the performance comparisons between different solvers and propeller designs are

Table 1

Summary of the propeller design and test conditions for the non-conformal HLP [48].

Design parameters:	
Radius (m)	0.288
Pitch angle at $0.75R$ (degrees)	27.4
Number of Blades (-)	5
Design condition:	
Rotational velocity (RPM)	4549
Flight velocity (m/s) (Sea Level)	29.84
Design performance:	
Thrust (N)	222
Torque (Nm)	21.62
Power (kW)	10.3

Table 2

Comparisons of predicted propeller performance for the non-folding and folding designs [47].

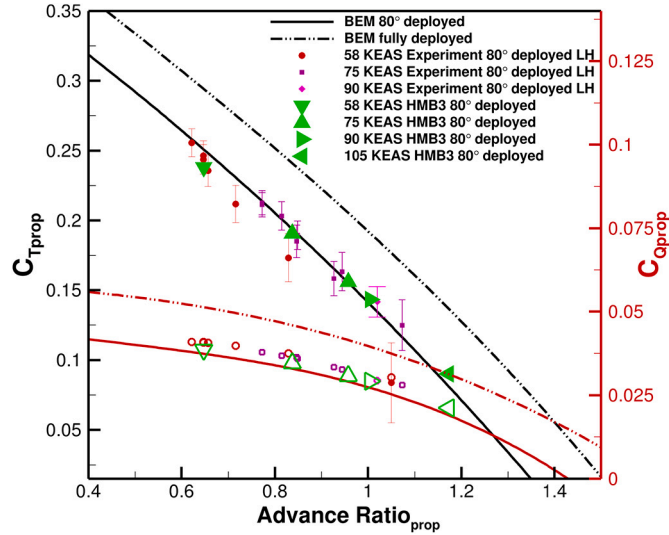| Propeller Design	Overflow	HMB3	Δ
Thrust (N)			
Non-conformal	222.0	222.2	0.1%
Conformal	217.0	217.6	0.3%
Torque (N.m)			
Non-conformal	21.50	22.42	4.2%
Conformal	20.80	21.97	5.6%

shown in Table 2. Good correlations can be found for different propeller designs and numerical methods.

In addition to the comparison of the results between different solvers, the validation was also carried out with the recent folding conformal HLP experimental results [45]. High performance take-off and landing conditions are presented in Table 3, and used for CFD calculations. Furthermore, the HLP was also investigated with a sweep of advance ratios to understand the performance at different flight conditions.

The HMB3 CFD solver was used to predict performance, as shown in Fig. 3. Aerodynamic coefficients were compared against the experiments with various advance ratios. Good agreement can be observed between the results from HMB3 and experiments. [45]

Table 3

Summary of the propeller design and take-off conditions for conformal HLP [45].

Design parameters:	
Radius (m)	0.288
Pitch angle at $0.75R$ (°)	24.1
Number of Blades (-)	5
Blade tip Reynolds number (-)	0.07×10^6
Design condition:	
Blade tip Mach number (-)	0.421
Rotational velocity (RPM)	4800
Flight velocity (m/s) (Sea Level)	29.84
Design performance:	
Propeller thrust coefficient (-)	0.238

Table 4

Summary of grid sizes used for the GARTEUR AG26 DLR 13x7 isolated rotor.

Grid Component (Isolated Rotor)	Grid 1	Grid 2	Grid 3
Rotor	4.7	6.0	7.0
Background	3.0	6.2	12.00
Total (million cells)	7.7	12.2	19.0

Table 5

Summary of grid sizes used for the GARTEUR AG26 DLR 13x7 rotor in tandem configurations.

Grid Component (Tandem Rotor)	Grid Cells
Rotor 1	4.7
Rotor 2	4.7
Local Refinement 1	0.8
Local Refinement 2	0.8
Near-field	22.0
Far-field	0.8
Total (million cells)	33.8

Table 6

Summary of the grid sizes used for the WIPP cases.

Grid Component	Cells (Millions)
Background	1.17
Local refinement	5.29
Wing	30.75
Tip propeller	30.32
Total	67.50

Table 7

Summary of conditions for Case 180 of WIPP.

Wingtip-mounted propeller:	
Pitch angle at $0.7R$ (degrees)	19.5
Test conditions:	
Free-stream Reynolds number (-)	0.08×10^6
Free-stream Mach number (-)	0.08
Rotational velocity (RPM)	8060
Target performance:	
Thrust coefficient (-)	0.4

Fig. 3. Validation of HMB3 solver for the conformal HLP. Empty symbols represent the respective torque coefficients. (Blade Element Momentum (BEM) and experimental data are from Litherland et al. [45].)

3.2. Multi-rotor systems - GARTEUR contribution

Regarding the aerodynamic and acoustic characteristics of multi-rotor systems, the GARTEUR Action Group HC/AG-26 has been established and coordinated by DLR. Fourteen partners from civil and military authorities, representatives of the European industry, research establishments, and academia are participating in the group's activities. One of the objectives of AG26 is to gain knowledge about noise generation and noise propagation of multi-rotor systems, including installation effects. The first common test campaigns, involving PIV measurements, were carried out by CIRA/DLR [50] using DLR's small rotor configuration. Further wind tunnel tests also included aerodynamic performance and acoustics of isolated and tandem rotor configurations [51–53].

Fig. 4 illustrated the grid topology used for the cruise simulations with isolated and multi-rotor systems. To understand the sensitivities of the rotor performance to the CFD grid, a mesh convergence study was performed on the full rotor, in axial flight, as shown in Table 4 (also see Table 5 for tandem rotor configurations grids and their component sizes). A grid sensitivity study was shown negligible differences in loads below the three employed grids.

For the DLR experiments, the aerodynamic loads [54] from HMB3 are cross-plotted with experimental data [46] in Fig. 5. Additionally, the velocity field was averaged over one revolution, like the PIV data from CIRA/DLR [50]. Extracted distributions from -0.1R to -0.6R below the rotor, in Fig. 6, show similar trends and good agreement with the PIV [50] (also see Fig. 7 for extracted distributions from -0.4R to -1.0R below the rotor, and for the tandem configuration). Furthermore, wake

profiles from a tandem configuration where two rotors had an offset in lateral and vertical, were extracted and compared with the PIV [46]. The agreement between the simulations and experiments from these two configurations confirmed the accuracy and reliability of the HMB3 CFD method in predicting the aerodynamic rotor performance.

3.3. Workshop for integrated propeller prediction (WIPP)

In an effort to bridge the knowledge gap in propeller/wing interactions, the wingtip-mounted propeller (WIPP) tests in the Lockheed Martin low-speed wind tunnel (LSWT) were conducted [44]. The test model of the WIPP featured a semi-span wing measuring 1.7 meters (67 inches), and a wingtip-mounted C-130 propeller scaled at 10% of the actual size. Detailed measurements of forces and moments were collected at various angles of attack and thrust settings.

To this end, before studying the propeller wing interaction for DP systems, the WIPP case was compared to verify that HMB3 has the ability to predict associated flows. The geometry and the computational domain for the WIPP cases [55] is shown in Fig. 8. In addition, the mesh size and the computational setup applied are shown in Tables 6 and 7.
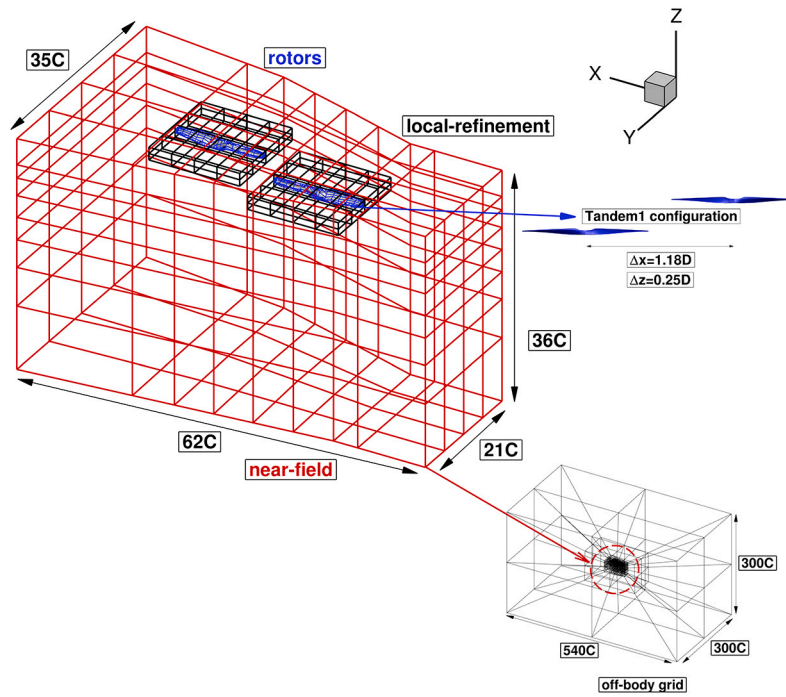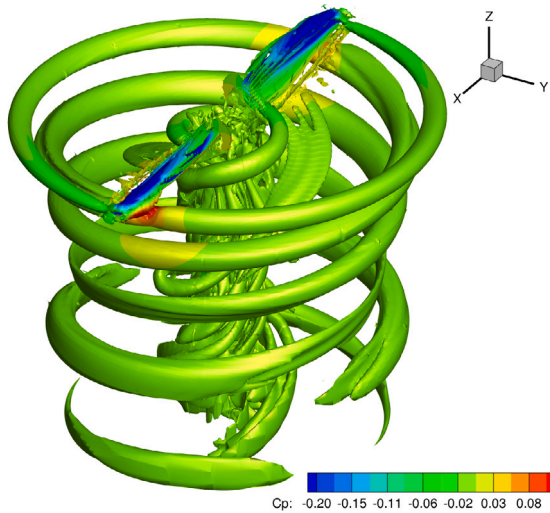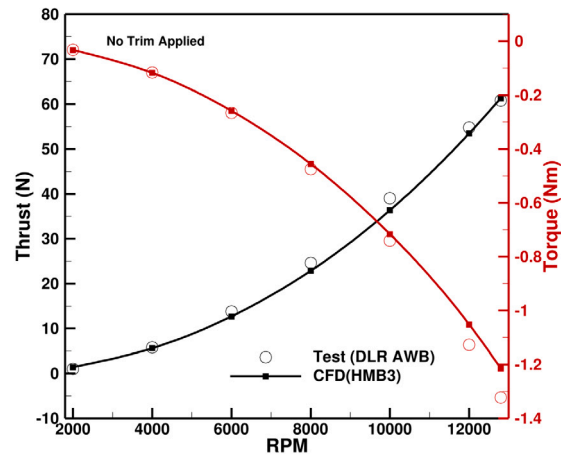
Fig. 4. Grid topology used for HMB3 simulations of the GARTEUR AG26 multi-rotor cases.

(a) Wake visualisation at RPM 12,000.

(b) Thrust and torque comparison.

Fig. 5. GARTEUR AG26 13x7 isolated rotor flow visualisation and performance for RPMs between 2,000 and 12,800, compared between HMB3 and measurements from [46].

Using the tip-mounted propeller geometry of the WIPP project for the current study, the CFD method was validated against experimental data [55]. The selected test cases were referenced as Cases 79, and 180 in the experimental report [55], with their conditions are presented in Table 7.

More analyses involved extracting wing loading, surface pressure (see Fig. 9) and wake profile (see Fig. 10) data at the highest selected thrust and Mach number conditions. Using resolved blades, the wake profiles at 0 degrees of wing angle of attack, are compared at two distances in Fig. 10. Comparing the propeller wake at distances of +19.95 and +16.45 inches ahead of the trailing edge of the nacelle showing good agreement with the experimental data. Due to the unsteadiness of the wake, time averaged CFD results were provided and compared with test data.

In addition, in comparing the surface pressure coefficients at 2 degrees of wing angle of attack, the surface pressure data from various extracted locations at BL 60.75 and BL 57 are presented and compared in Fig. 9. These locations were chosen, because the BL 60.75 strip is nearest to the impinging propeller tip vortex, and BL 57 is outside the propeller slipstream. From the sliced surface pressure coefficients, it can be seen, that the most interesting station is BL 60.75 of Fig. 9(a), that is directly influenced by the propeller tip vortex. In comparison to BL 57, a significant increase in the suction peak and stagnation pressure was observed due to the propeller wake.

The validation studies presented in this section demonstrated that the propeller wake and wing interaction were accurately predicted, and resolved. This justifies using the HMB3 methods for predictions of the propeller, wing loads and associated flow phenomena.
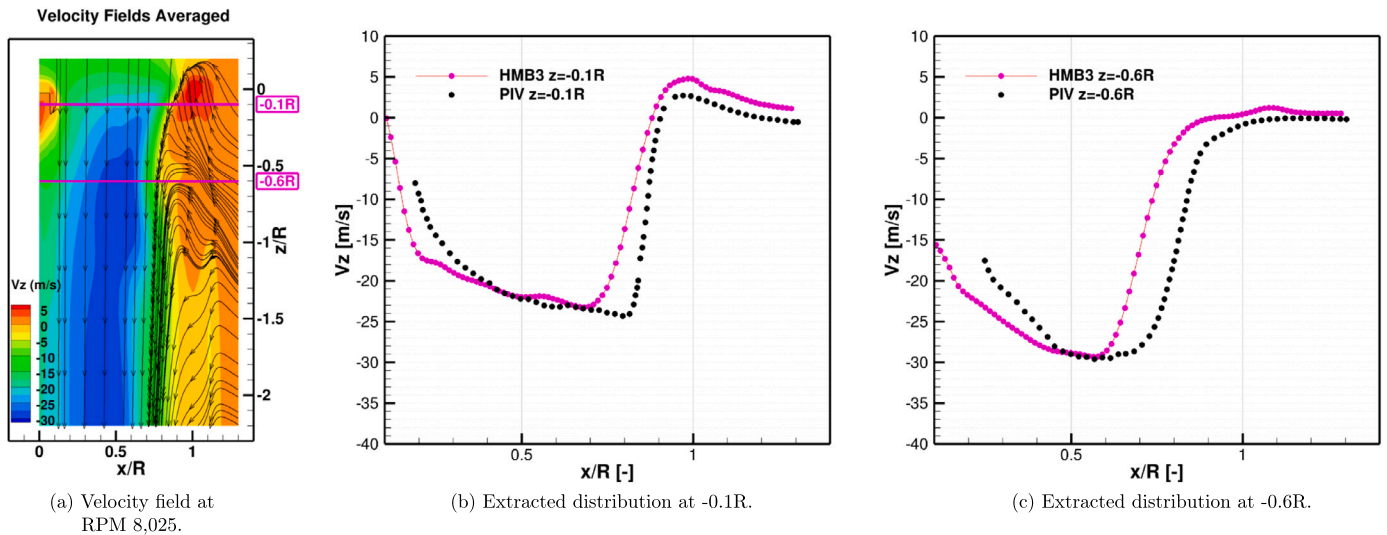
(a) Velocity field at RPM 8,025.

(b) Extracted distribution at -0.1R.

(c) Extracted distribution at -0.6R.

Fig. 6. (a) Averaged velocity field results from HMB3. (b)(c) Extracted velocity distributions from the wake region at distances of -0.1R and -0.6R below the isolated rotor, compared with PIV [50].
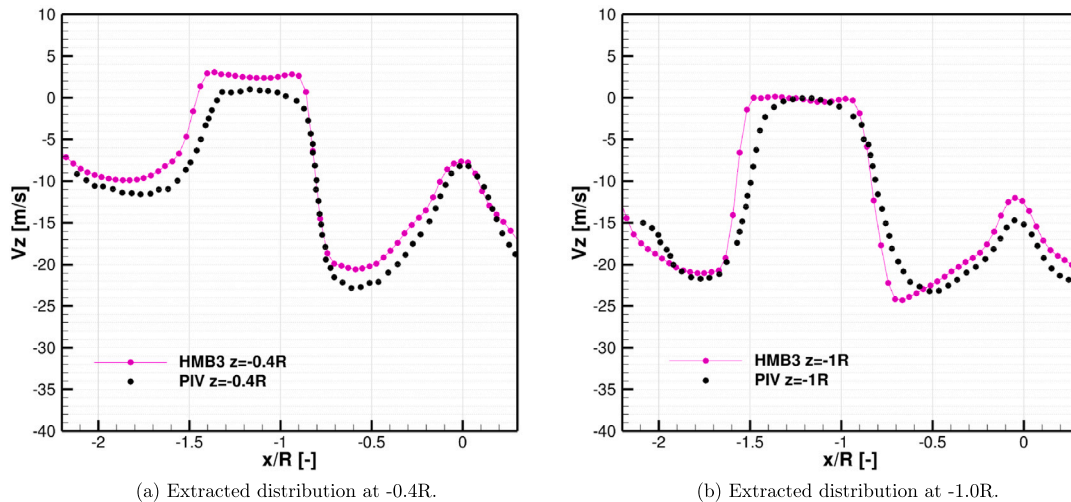

(a) Extracted distribution at -0.4R.

(b) Extracted distribution at -1.0R.

Fig. 7. Extracted velocity distributions from the wake region at distances of -0.4R and -1.0R below the tandem rotors, compared with PIV [50].

4. Optimal distribution of propellers

4.1. Single auxiliary propeller

An optimised DP system was studied using the actuator disk method, and a Kriging model [56], based on the WIPP geometry. The smaller propellers were scaled to match the overall size of the X-57. The initial study focused on positioning a single propeller to maximise the lift-to-drag ratio of the wing. The effectiveness of the auxiliary propeller was evaluated at nine locations along the wingspan, and above/below the wing.

Fig. 11, shows the results for the lift-to-drag ratio across the examined region. The propeller positioned above the wing yields the highest lift-to-drag ratio over the nine positions analysed. This agrees with trends reported in the literature [8,9,57], and is a result of the acceleration of the flow over the upper surface of the wing, which increases the suction. Placing the propeller at the highest position above the wing, reduces the drag force acting on the wing by preventing the wake from fully impacting on the wing. While relocating the propeller below the wing would also decrease the drag, it would not cause flow acceleration over the suction side, thus diminishing the lift increment. The study found that there is minimal disparity between the three spanwise locations tested across all vertical heights.

4.2. Multiple auxiliary propellers

Subsequent studies concentrated on the overall performance of the complete DP setup and how the placement of propellers affected it, as illustrated in Fig. 12(a). The propeller parameters and the operating conditions for the current study are detailed in Table 8. The six auxiliary propellers were uniformly distributed across the wingspan, and situated ahead of the wing's leading-edge at a minimal distance of 0.04 m. This corresponds to the tip chord length of the wingtip propeller, as represented by the dash-dot line in Fig. 12(a). The distributed propellers were relocated to different positions, as illustrated by the red points in Fig. 12(a), and the corresponding performance changes were evaluated through CFD calculations. Kriging response surfaces were then constructed based on the variation of locations in wing chord-wise and vertical directions, and respective CFD results to analyse the performance alterations cased by the propeller placements.

During this study, all six propellers were relocated to different positions while maintaining their relative positions to each other. Fig. 12(b) illustrates the range of the studied propeller positions at a wing section. The parametric investigation included alterations in position along the x- and z-directions. The longitudinal and vertical displacements, with respect to the initial configuration, were normalised using the auxiliary

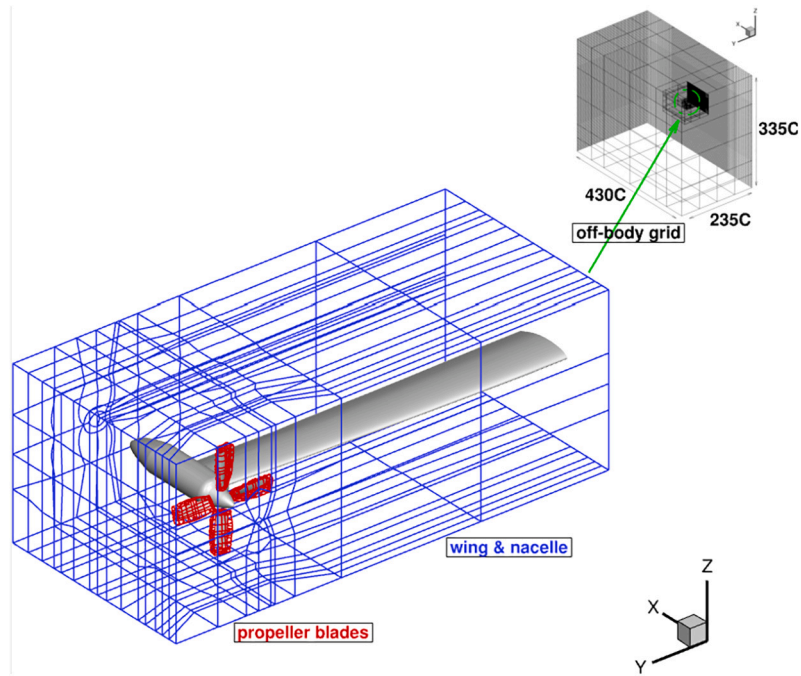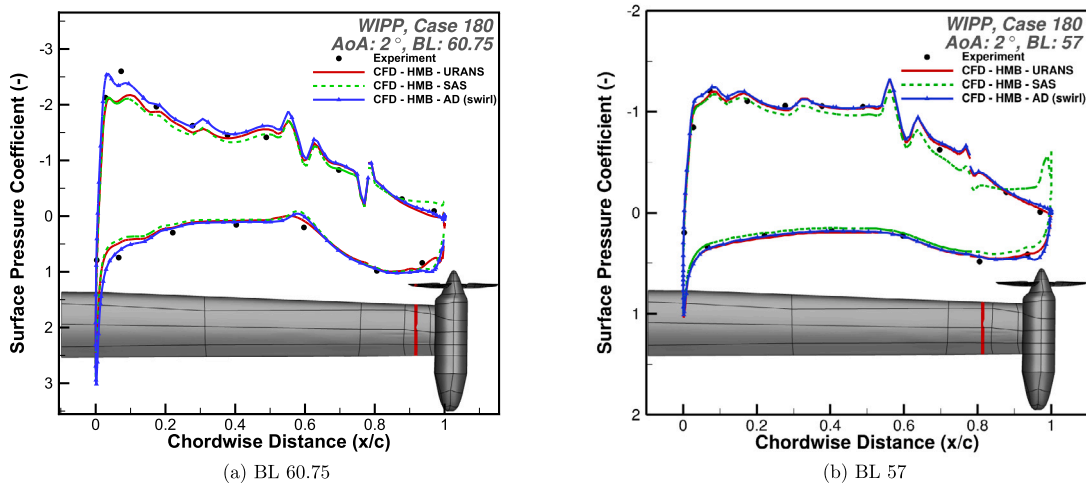**Fig. 8.** Grid topologies employed for the WIPP cases.

(a) BL 60.75

(b) BL 57

Fig. 9. Comparison of the surface pressure results between experiments and CFD.
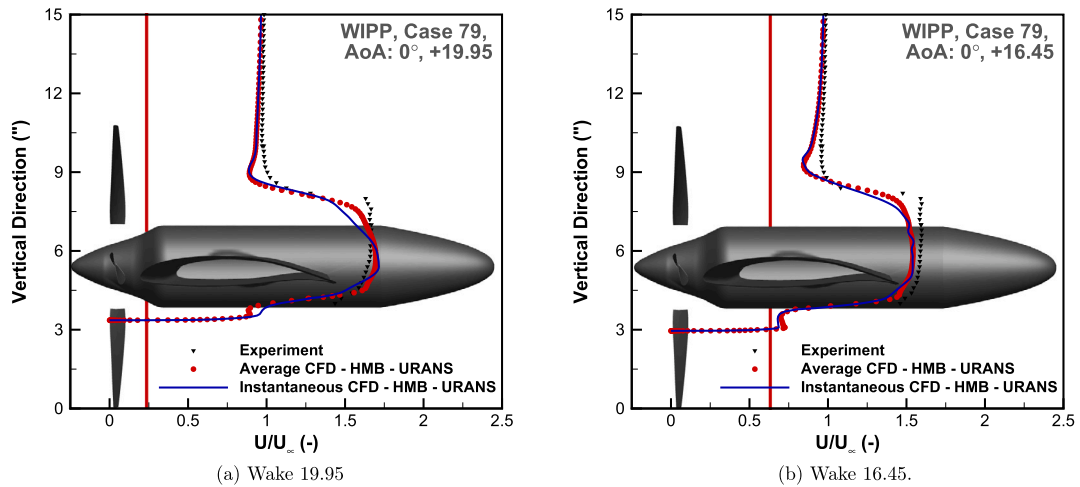

(a) Wake 19.95

(b) Wake 16.45.

Fig. 10. Comparison of the wake profiles between experiments and CFD.
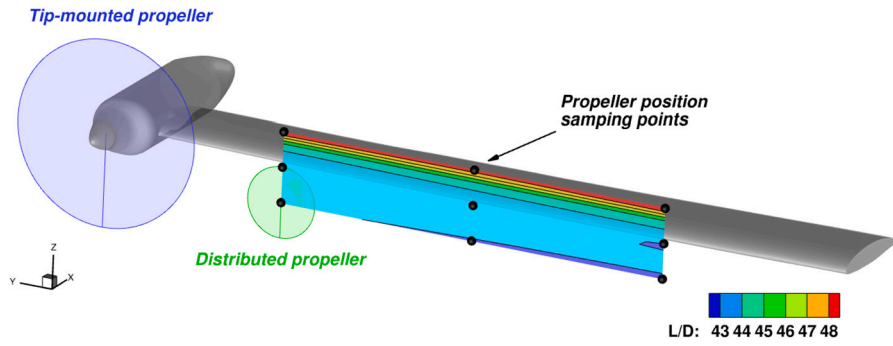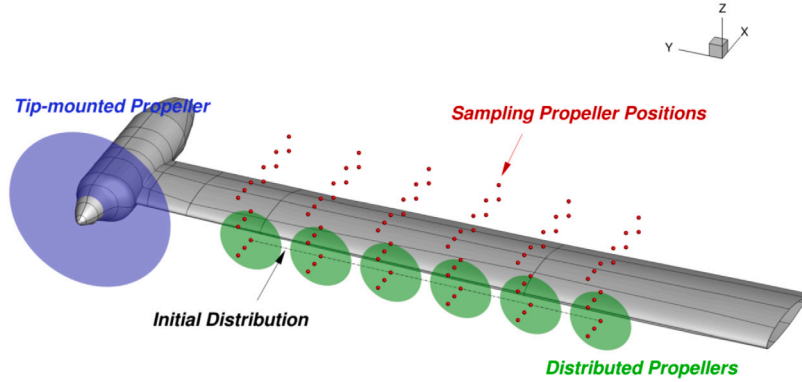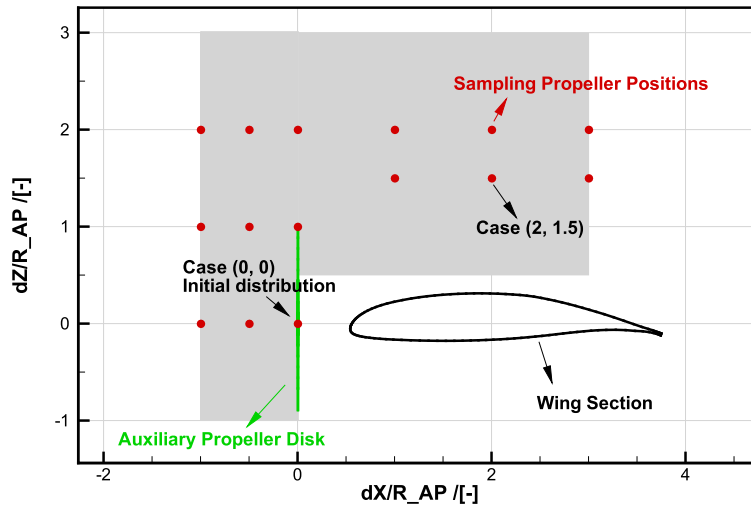
Fig. 11. Optimisation for a single propeller.

(a) Illustration of the studied DP configuration and the sampling propeller positions.


(b) Investigated range of the propeller positions at a wing section. The x and z changes were normalised using the auxiliary propeller radius R_{AP} based on the WIPP wind tunnel scale. The grey area represents the boundaries of the propeller disk.

Fig. 12. Locations of the actuator disks around the wing.

blade radius (R_{AP}) which is scaled based on the WIPP experimental size. A total of fifteen sampling points were examined, which included the initial baseline position. Each instance was designated by a coordinate, representing its displacement from the initial location, as shown in Fig. 12(b).

It is important to note that the span-wise positions of the propellers could not be changed due to geometric limitations. As demonstrated by the study (see 4.1) involving a single propeller, positioning it below the wing would not enhance the overall performance. As a result, the current sampling sets concentrated on positions above the wing, and along the stream-wise directions.

In reduced order simulations from this section, all propellers were modelled using actuator disks. Figs. 13(a) to 13(c) present the surface pressure solutions of three tested configurations, including the baseline configuration with only the tip-mounted propeller. Subsequent analyses were focused on the performance variations relative to the baseline scenario. The distributed auxiliary propellers were assigned sequential numbers ranging from 0 to 5, from the outboard to the inboard direction. It was observed that the introduction of distributed propellers, and their placements, caused differences in the flow patterns. In the baseline solution, there was a single section of high suction pressure (indicated by dark blue) downstream the tip propeller, which remained

(a) Baseline configuration without auxiliary propellers.
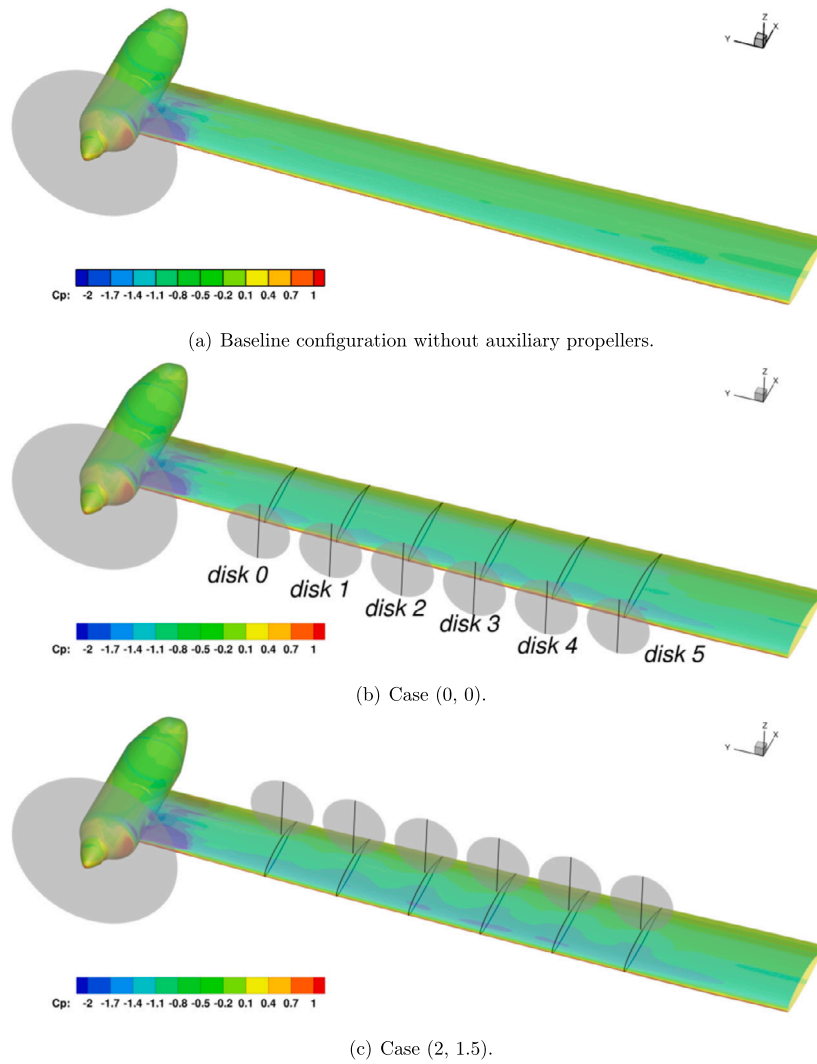
(b) Case (0, 0).

(c) Case (2, 1.5).

Fig. 13. Surface pressure comparisons between the baseline configuration, the lowest L/D configuration case (0, 0), and the highest L/D configuration case (2, 1.5). The distributed auxiliary propellers were numbered from 0 to 5 from the wing tip to root.

Table 8
Parameters and operating conditions of the DP configuration employed in the optimisation using the actuator disk method.

Free-stream velocity (m/s)		27.22
Angle of attack (degrees)		2.09
Tip-mounted propeller:		
Propeller C_T, C_Q		0.038, 0.0098
Auxiliary propellers :		
R_{AP}	(m)	0.0782
R_{TP}	(m)	0.2058
R_{AP}/R_{TP}		0.38
Propeller C_T, C_Q		0.015, 0.004
Formation		Even distribution along wing span

consistent in all other cases. However, the installation of the auxiliary propellers increased the suction pressure towards the leading edge of the wing, compared to the baseline. In particular, for the case at (2, 1.5), the extent of the amplified suction pressure was observed to be more prominent across the upper surface of the wing, with disks 2 and 3 located almost at mid-chord.

The alterations in wing lift and drag due to the changes in position of the distributed propellers are presented in Figs. 14(a) and 14(b). The lift and drag alterations were standardised by the corresponding values of the baseline configuration, where only the tip-mounted propeller was used. With respect to lift, the installation of distributed propellers increased the wing lift across the entire range of positions examined. The highest lift augmentation, which was approximately 15%, was achieved when the propellers were placed in front of the wing, or close to the trailing edge and above the wing. On the other hand, the lowest lift increment, which was around 3%, occurred when the propellers were located further upstream, and considerably above the wing, where the wing could barely benefit from the propeller slipstream. The wing experienced a rise in drag of around 35% together with the lift increase when the propellers were positioned in front of the leading edge. Conversely, when the propellers were placed above the wing near the middle chord (such as in Case (2, 1.5)), the wing drag was reduced by roughly 35%, while the lift was augmented by approximately 12%.

Fig. 14(c) further presents variations of the wing lift-to-drag ratio brought in by the propeller position changes. As expected in Figs. 14(a) and 14(b), the overall wing efficiency was reduced, when the propellers were placed upstream of the wing. Case (0, 0) (see Fig. 12(b)) shows the largest lift-to-drag ratio reduction of about 10% compared to the baseline case. As the propellers were moved downstream, and placed above the wing, the wing efficiency was increased due to the increased lift and reduced drag. Case (2, 1.5), of Fig. 12(b), showed the maximum lift-to-drag ratio increase of about 80% compared to the baseline case within the range studied.

(a) Lift variations.

(b) Drag variations.

(c) Lift-to-drag ratio variations.
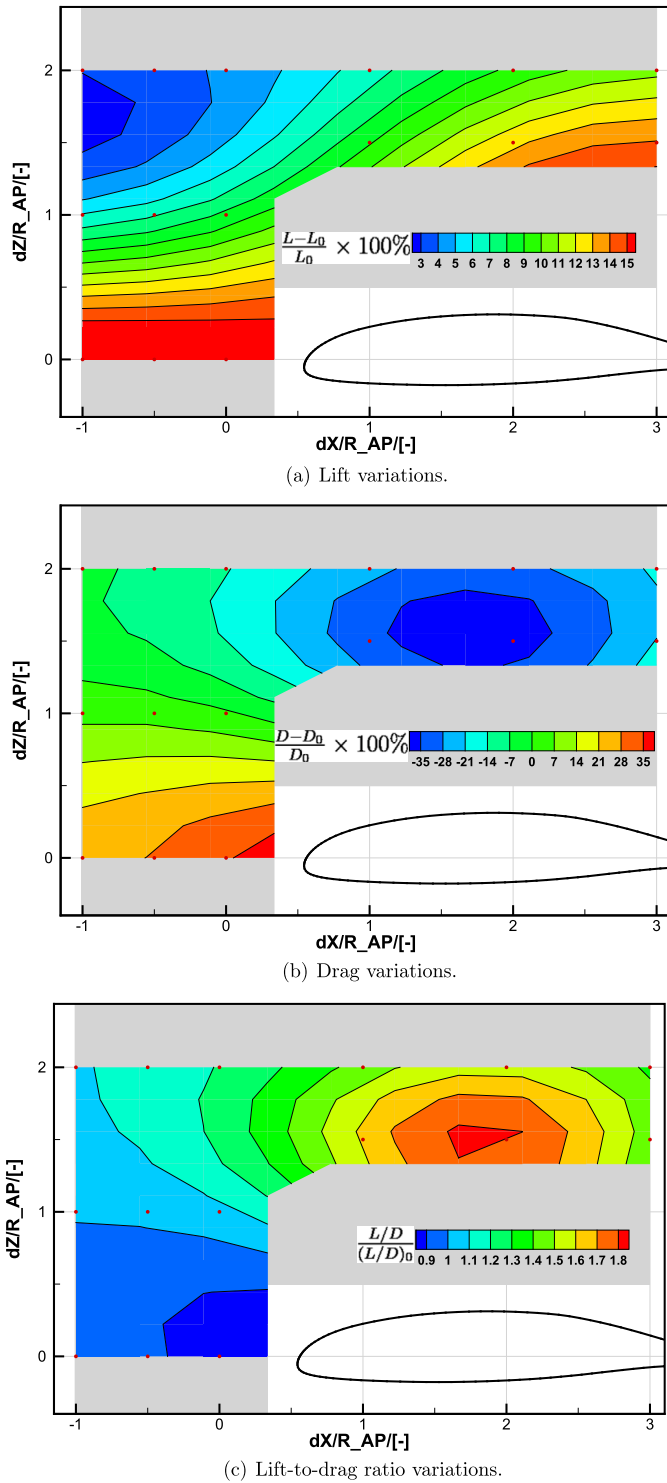
Fig. 14. Wing lift, drag, and lift-to-drag ratio variations due to position changes of the distributed propellers. The x and z changes were normalised using the auxiliary propeller radius R_{AP} based on the WIPP wind tunnel scale. The lift and drag changes were normalised using the baseline values. The grey area represents the boundaries of the propeller disk.

Further comparisons between the baseline case, the least and most efficient configurations (Cases (0, 0) and (2, 1.5) of Fig. 12(b)) among the tested sampling set were conducted to understand the differences. Fig. 15 shows the sectional surface pressure distribution of the wing, at a slice passing through the innermost propeller disk (disk 5 of Fig. 13(b)).
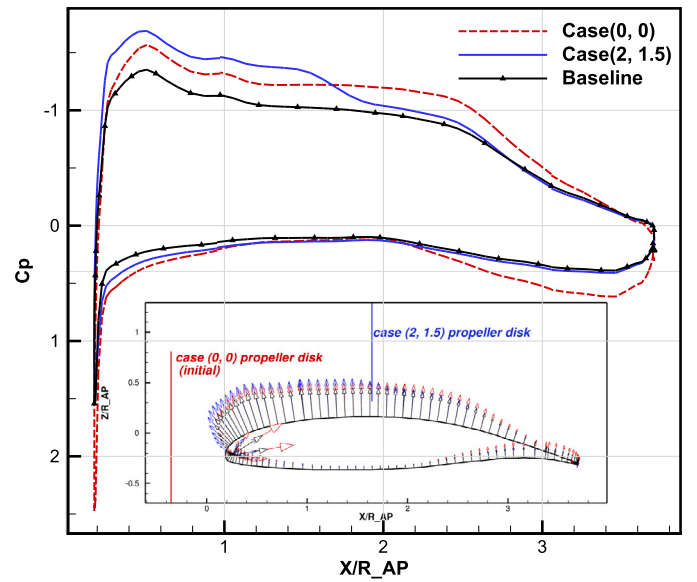
Fig. 15. Sectional Cp distributions and pressure force vectors comparing the baseline case, lowest L/D case (Case (0, 0), and highest L/D case (Case (2, 1.5)). The wing section through the inner-most auxiliary propeller (disk 5) is shown.

Compared to the baseline case, the pressure distribution of Case (0, 0) with the propellers in front of the wing leading edge showing decreased pressure on the suction side, and increased pressure on the pressure side, resulting in an overall increase in lift and drag. This effect is similar to increasing the free-stream velocity for the wing section. In contrast, for Case (2, 1.5) where the propellers were placed above the wing near the middle chord, the wing leading-edge suction was enhanced upstream of the propeller, and the pressure was slightly recovered through the propeller disk. These changes led to reductions in drag, and increases in lift, although the lift increment was less significant than that observed for Case (0, 0).

The sectional pressure force vectors presented in Fig. 15 illustrate the surface pressure differences, and the impact on the forces for the three cases. It is evident that placing the propellers upstream of the wing resulted in a strong stagnation area at the leading-edge, contributing to drag forces. However, moving the propellers above the wing enhanced the suction around the upper leading edge, and slightly recovered the pressure after the propeller disk, leading to reduced drag forces. In comparison to the baseline case without the distributed propellers, both cases showed increased suction forces on the upper surface and pressure forces on the lower surface, resulting in increased lift forces.

5. Verification of propeller installed configurations

In the preceding section on optimisation, the reduced-order method was utilised to approximately locate the optimal position of the distributed propellers. Nevertheless, the actuator disk method failed to capture the unsteadiness of the actual propeller wake, which has an impact on the propulsion system. In addition, the performance of the propulsion system changes due to different installation effects. Furthermore, additional surfaces from nacelle and pylon structures, will also have impact on the propulsion system. Therefore, additional verification cases utilising high-fidelity methods are necessary. These investigations should include a single isolated propeller, installed tractor propeller, OTW and OTW with pylon configurations as shown in Fig. 16. The condition investigated across all cases is shown in Table 9, and the employed grid topology and size are presented in Fig. 17, and Table 10.

Verification studies using high-fidelity methods covered the baseline of the isolated HLP, installed in tractor, OTW, and pylon installed OTW configurations, as shown in Fig. 18. All these cases were tested at the
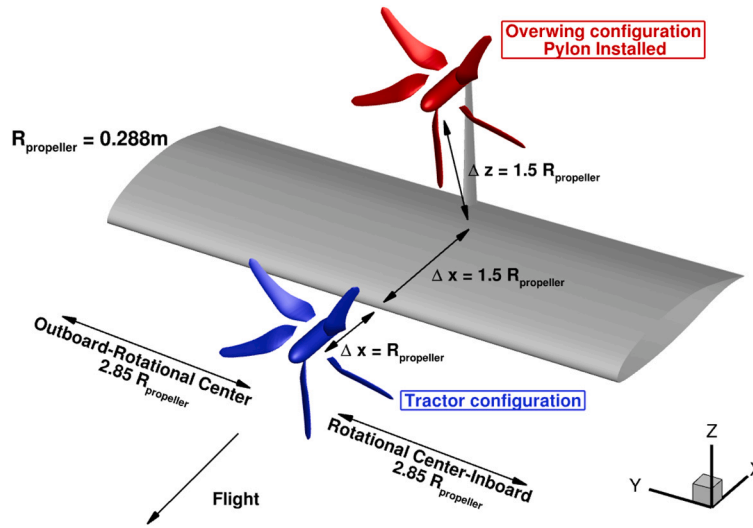
Fig. 16. Schematic of tractor and OTW configurations, and the OTW configuration with pylon installed. A full scale of X-57 aircraft with $R_{propeller}$ equal to 0.288 m and its corresponding lifting surface are used in all verification cases.
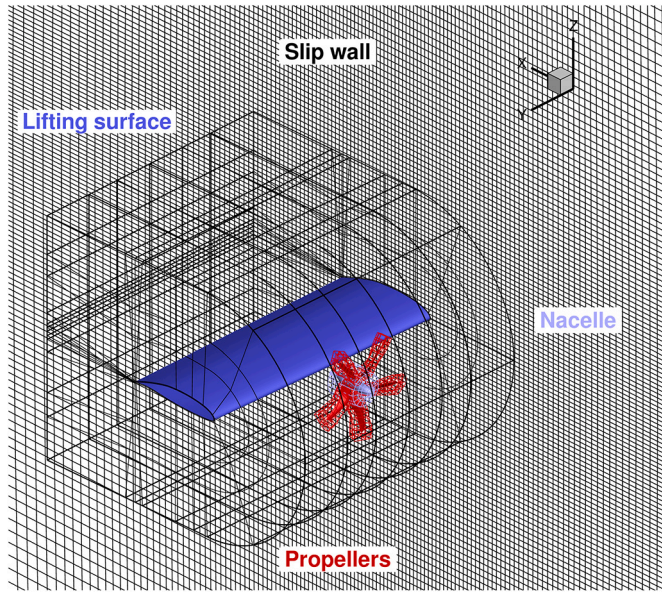

Fig. 17. Chimera grid, and topology used for installed configurations.

Table 9
Summary of the computational setup for distributed propellers.

Freestream Reynolds number (-)	0.2×10^6
Freestream Mach number (-)	0.08
Rotational velocity (RPM)	4800
Pitch angle at $0.7R$ (degrees)	27.52

Table 10
Summary of the grid size for single, installed, HLP.

Grid Component	Cells (Millions)
Background	2.3
Lifting surface	44.5
Spinner	5.7
Distributed propeller	13.5
Total	66.0

same free-stream speed, pitch angle and rotational speed. Installing the propeller in front of the leading edge, a higher pressure region can be found after the propeller. The pressure recovered earlier compared to the isolated propeller and OTW configurations due to the swirl recovery from the wing and stagnation. In addition, placing the propeller OTW, further accelerates the flow along the upper surface of the lifting wing, and a higher suction region is formed. However, the accelerated flow speed at the OTW configuration, which in turn changes the effective advance ratio, adds more loading to the propeller and there are no swirl recovery, and stagnation area from the wing.

At high loading and at an advance ratio (μ) of 0.19, it was discovered that the interactions between the propeller and the lifting surface had a much greater impact on the local performance of the lifting surface. Under identical conditions, the OTW configuration experienced an increment of around 1.3% in lift, and roughly 3 times more in lift-to-drag ratio compared to the tractor configuration, due to the drag reduction (see Table 11). This decrease in drag is clearly visible in Figs. 19 and 20, as the OTW configuration displayed a higher suction peak and pressure recovery compared to the tractor configuration. On the other hand, the tractor configuration exhibited a more significant suction peak downstream the propeller, as the velocity from the upper surface had increased significantly due to the propeller, and the pressure failed to recover as in the OTW configuration. Additionally, on the lower surfaces, the tractor configuration was significantly affected by the slipstream from the propeller and resulted in the formation of a high pressure gradient in the chord-wise direction. The propeller performance of the OTW configuration dropped by 6.4% due to the thrust penalties. However, due to the great benefit from the lifting surface, the overall propulsive efficiency has increased by 5.5%.

Similar benefits can also be found in the OTW configuration with pylon installed. Trimmed results showed that 3.9% more lift has been generated, and the benefit of the lift-to-drag ratio was 130%, as the drag increased due to the pylon structure. In addition, propeller performance benefited slightly by the installed pylon structure in the OTW configuration which has a swirl recovery effect. Nevertheless, the overall aerodynamic performance of the OTW configuration with/with-out pylon installed was increased.

6. Investigation of optimised distributed propulsion systems

This section presents further investigations into different DP systems with multiple propellers installed. The setups for these propulsion systems are given in Fig. 21. The installed HLP was previously validated in section 3 [33], and the lifting surface was extracted from the
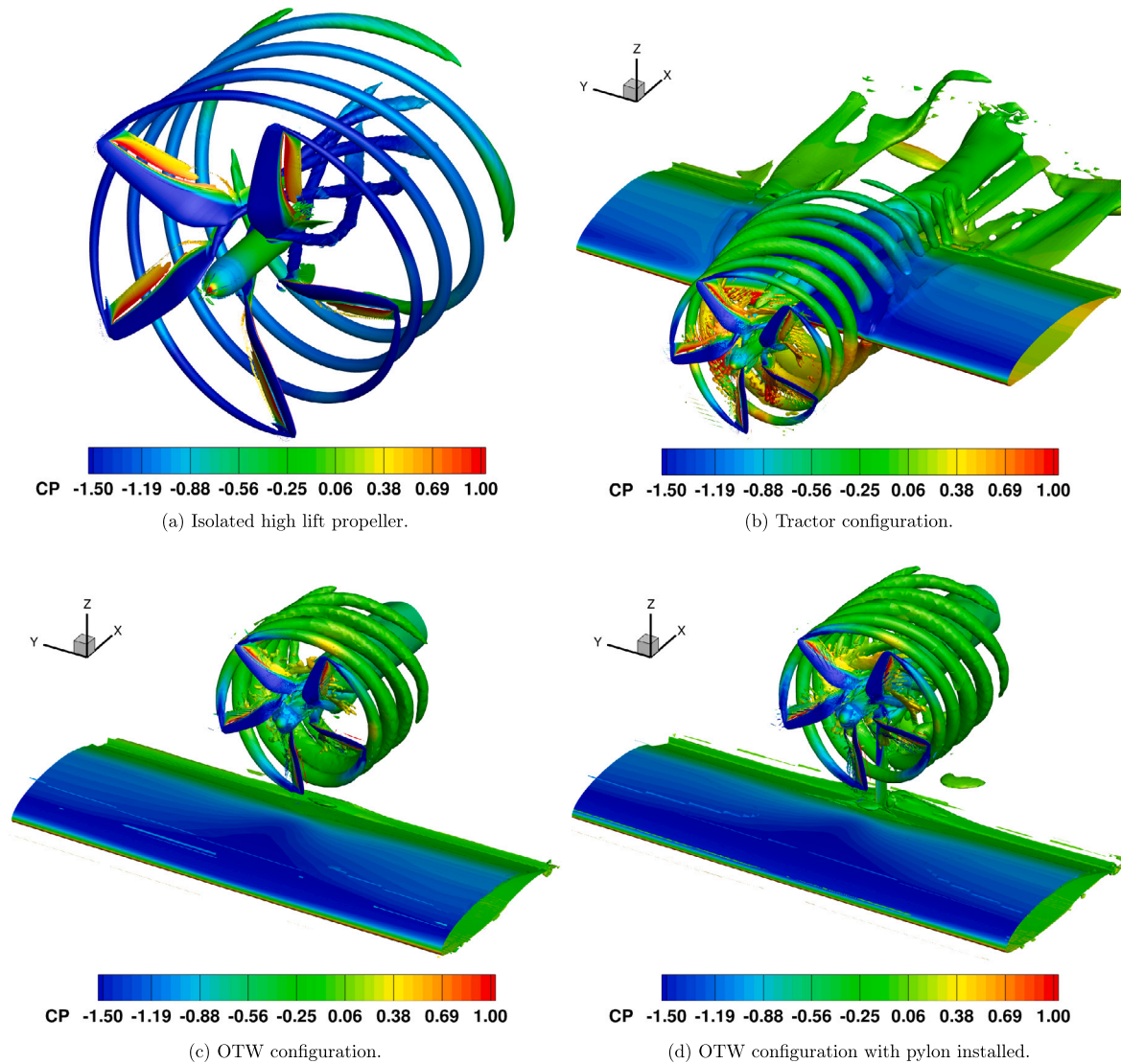
(a) Isolated high lift propeller.

(b) Tractor configuration.

(c) OTW configuration.

(d) OTW configuration with pylon installed.

Fig. 18. Isolated and installed propeller wake visualisation using iso-surfaces of Q-criteria at a value of 0.1, coloured using pressure coefficient for different configurations.

Table 11
Performance comparison of single-propeller, installed, propulsion systems with multiple configurations.

Performance (RPM = 4800)	Tractor	OTW	OTW+Pylon	Benefit OTW	Benefit OTW+Pylon
Lift (N)	582	590	605	+1.3%	+3.9%
L/D (-)	15.2	60.0	35.0	+294%	+130%
Thrust (N)	257	238	241	-7.4%	-6.2%
Power (kW)	12.60	12.50	12.58	-0.8%	-0.2%
Propeller Froude efficiency (-)	0.56	0.52	0.53	-6.4%	-5.8%
Overall propulsive efficiency (-)	0.476	0.502	0.489	+5.5%	+2.7%

NASA X-57 cruise-efficient wing, which has also been used in previous WIPP studies [32]. Given the increased complexity of the aerodynamic interactions with increased number of installed propellers, this paper has also investigated multi-rotor validation cases, see section 3.2 [54]. With confidence in using the same CFD tools and grid resolution from the validation studies, the work focused on studying the aerodynamic performance of distributed tractor and OTW propulsion systems at the optimised propeller locations in full scale.

The investigation of DP systems started with assessing the performance of the tractor and OTW configurations with two propellers installed. The setup and the corresponding flow field are depicted in Figs. 21(a) and Fig. 23. Aerodynamic loads from the overall propulsion system and their individual components are presented in Table 12 and Fig. 24 (b). The results show that the benefit in lift-to-drag ratio is still present for the OTW configuration. Although the propeller performance drops in the OTW configuration, the overall propulsive efficiency is almost 4% higher than the tractor propulsion system.

Furthermore, by distributing the thrust from single to two propellers, the vorticity magnitude shown in Fig. 22 demonstrates a sig-
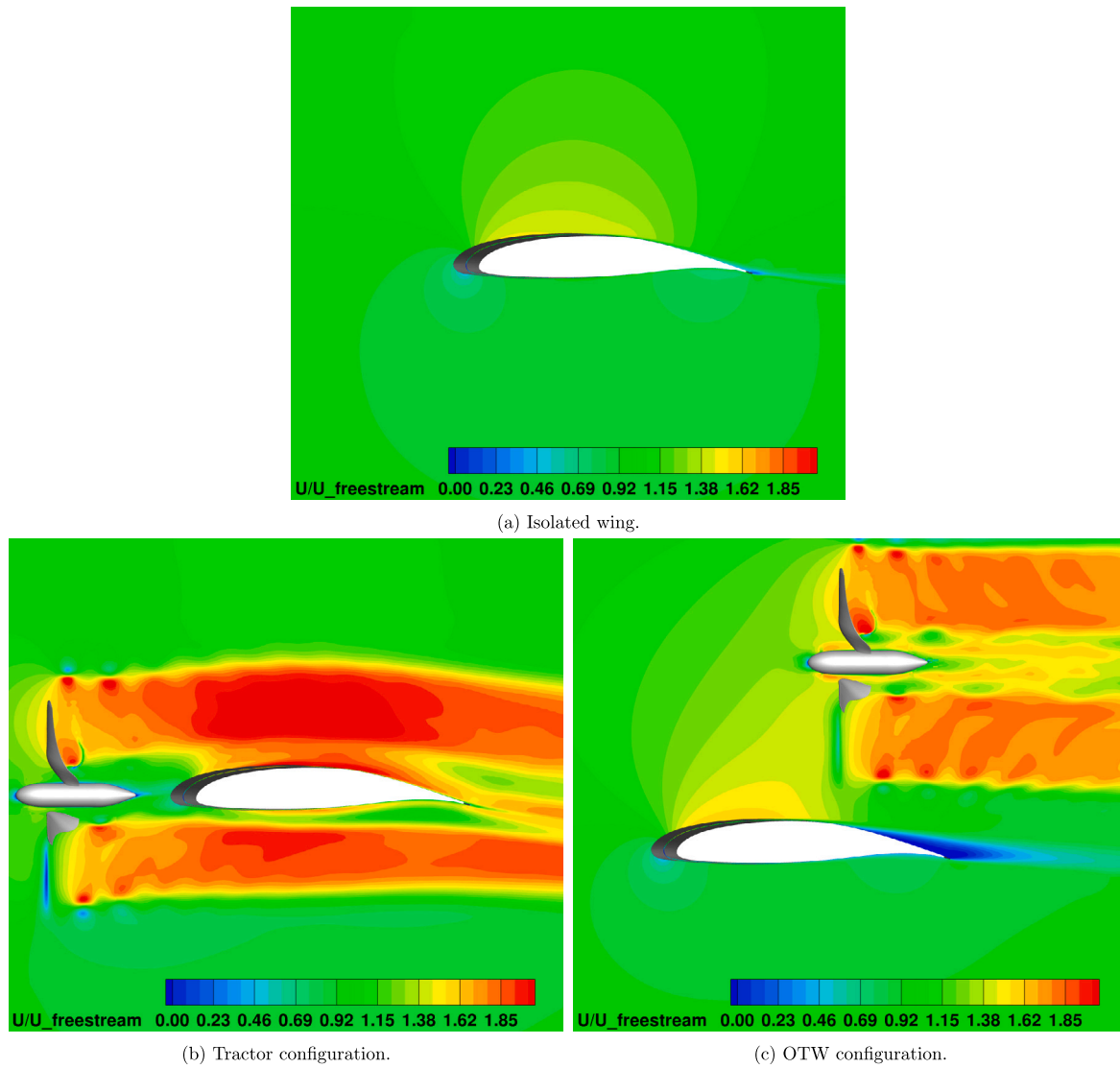
(a) Isolated wing.

(b) Tractor configuration.

(c) OTW configuration.

Fig. 19. Instantaneous axial flow speed (normalised using the far-field speed) for different configurations.

Table 12
Performance comparison of different two-propeller, installed, DP configurations.

Performance (RPM = 3900)	Tractor	OTW	Benefit of OTW
Lift (N)	1140	1149	+0.7%
L/D (-)	15.74	30.20	+92%
Thrust (N)	308	273	-11.3%
Power (kW)	13.3	12.8	-3.8%
Propeller Froude efficiency (-)	0.64	0.59	-7.8%
Overall propulsive efficiency (-)	0.487	0.505	+3.8%

nificant reduction in vorticity. This results in a lower tip speed for the DP system, which is important as the propeller/rotor performance and noise are highly dependent on the tip speed.

This work demonstrated that the single and two-propeller installed OTW configuration outperforms the conventional tractor configuration. However, a study conducted by Reynard et al. [11] found 1.5% drop in performance for the middle propeller when adjacent propellers were separated by 5% R. To this end, the current work also investigated three-propeller tractor and OTW configurations with a 40% R separation distance, between adjacent propellers. Propellers 1 and 3, visualised in Fig. 21, exhibited identical performance. However, Propeller

2, that is located most inboard, showed almost 1% better efficiency than the other two propellers. This performance difference, under the same separation distance, RPM, and rotation direction for all three propellers, was not observed in the two-propeller OTW configuration. This discrepancy may be attributed to the taper lifting surface, which was extracted from the X-57 cruise-efficient wing. Furthermore, as our work also investigated the equivalent three-propeller tractor configuration, a comparison of propeller performance at different locations revealed that propellers at locations 1, 2, and 3 showed identical performance. Therefore, the propeller performance from tractor configuration does not appear to be sensitive to the tapered lifting surface. Furthermore, as shown in Fig. 24(c), the performance benefits of the OTWDP system are maintained when compared to the equivalent tractor configuration.

With the optimal OTW DP system in place, further investigation incorporated a third propeller as shown in Fig. 21(b) and compared its performance with a one- and two-propeller OTW configuration, as presented in Table 13, and Fig. 24. Flow field visualisation of two- and three-propeller, installed tractor and OTW DP systems coloured using velocity are presented in Fig. 23.

As indicated in Fig. 24(d), compared to the two-propeller case, the three-propeller case generates more thrust than required power, resulting in a 2.6% higher propeller efficiency. Since the larger upper lifting surface area is affected by the slipstream of the three-propeller config-
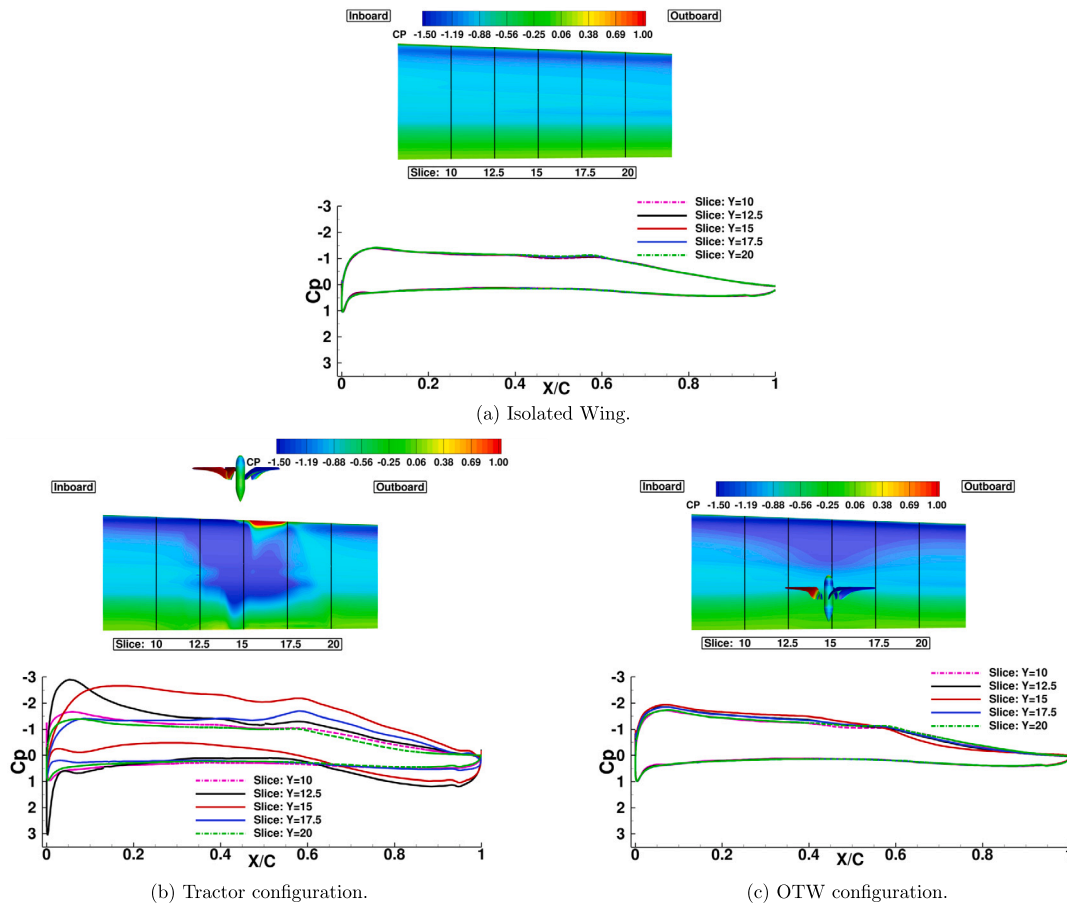
(a) Isolated Wing.

(b) Tractor configuration.

(c) OTW configuration.

Fig. 20. Extracted pressure coefficient distributions on the wing for the baseline, tractor and OTW configurations.

Table 13
Performance comparison of different OTWDP configurations.

Performance	One-prop	Two-prop	Three-prop	Benefit DP (2-3)	Benefit DP (1-3)
Lift (N)	1010	1083	1096	+1.2%	+8.5%
L/D (-)	24.4	35	38	+7.6%	+55.7%
Thrust (N)	240	273	353	+29.0%	+47.1%
Power (kW)	12.50	12.8	16.1	+25.8%	+28.8%
Propeller Froude efficiency (-)	0.527	0.586	0.602	+2.6%	+14.2%
Overall propulsive efficiency (-)	0.437	0.520	0.552	+6.2%	+26.3%

uration, there is 1.2% improvement in lift and a 7.6% increment in the L/D of the lifting surface. Furthermore, there is an overall improvement in propulsive efficiency by 6.2% for the three-propeller configuration.

When transitioning from a single-propeller to a three-propeller, installed DP system, as shown in Fig. 24(d), it was observed that the propellers become 14.2% more efficient. The L/D of the wing also increased by 55.7%, resulting in an additional 8.5% lift generation and 30.2% of drag reduction. In terms of overall efficiency, the three-propeller OTW configuration is 26.3% more efficient than the single-propeller installed OTW configuration, demonstrating the capability of a DP system to enhance the overall propulsive performance.

7. Conclusions

Based on the validation results presented, the location optimisation study of the DP, and the performance evaluation of DP systems, the following conclusions can be drawn.

The wingtip mounted propeller geometry from the WIPP project was simulated using CFD methods and compared with experimental data. A combination of resolved blade models and actuator disk models were employed in the CFD. The surface pressure coefficients, at critical wing stations, were found to be in good agreement between the CFD and experimental data. The resolved blade models captured the better wake effect across the wing, while the SAS method captured more of the wake downstream. However, the actuator disk models failed to capture unsteady effects, but were able to provide the average downwash effect of the disk.

In addition, this work conducted CFD simulations of rotors in isolated and tandem configurations, comparing them with the experimental database acquired during the development of the X-57 'Maxwell' electric aircraft, and from the GARTEUR AG 26 work. The results demonstrated that the simulation methods employed in this study effectively captured the performance and associated flow phenomena, particularly with strong rotor-rotor interactions.

Having established confidence in the employed CFD method, a single auxiliary propeller was evaluated to determine its optimal vertical
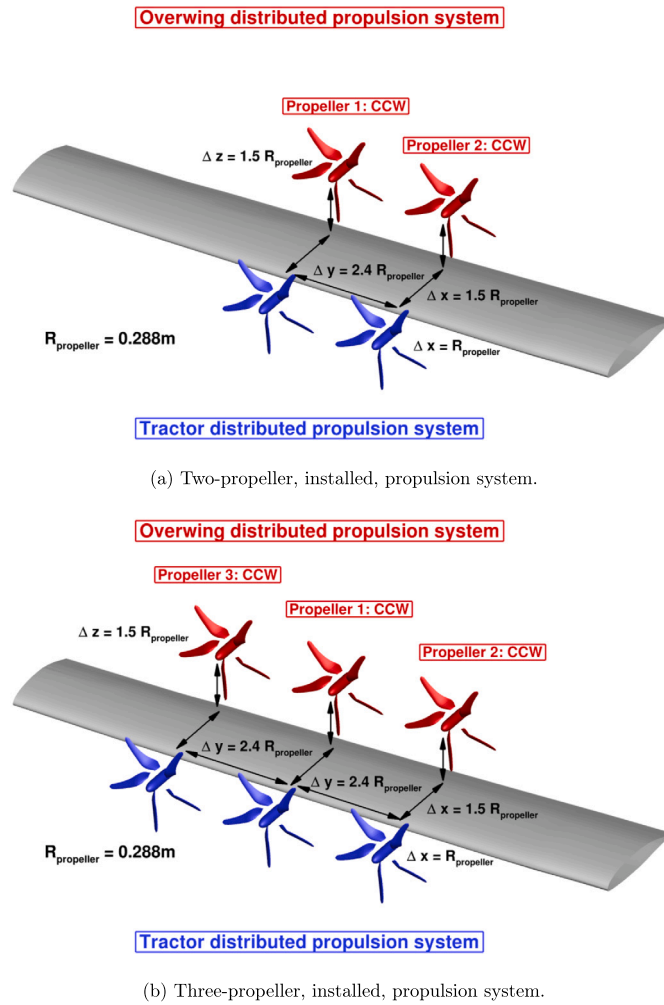
(a) Two-propeller, installed, propulsion system.

(b) Three-propeller, installed, propulsion system.

Fig. 21. Illustration of the investigated DP systems with multiple propellers installed. A full scale of X-57 aircraft with $R_{propeller}$ equal to 0.288 m and its corresponding lifting surface are used in all verification cases.
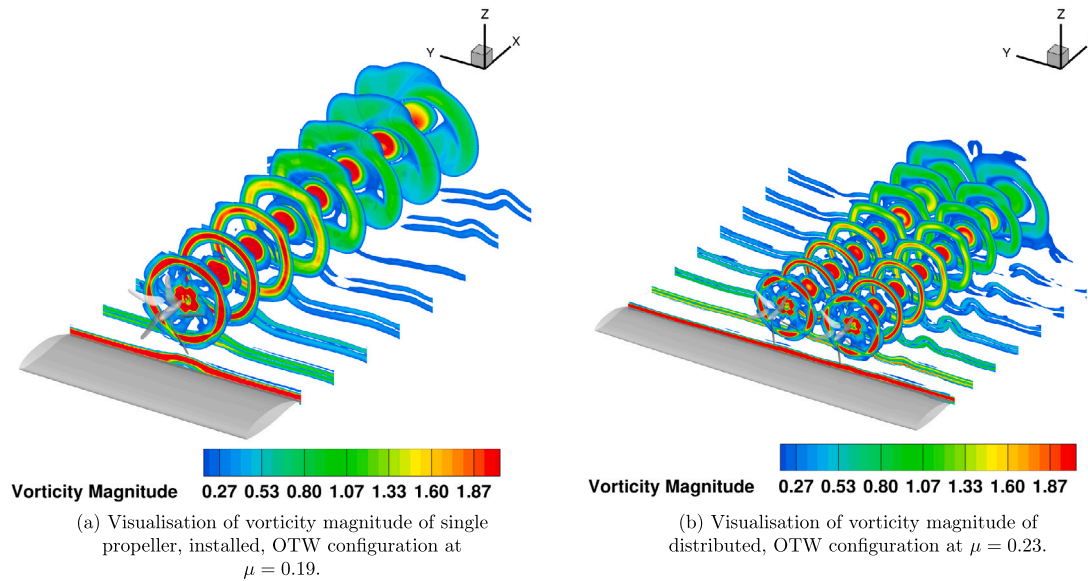

(a) Visualisation of vorticity magnitude of single propeller, installed, OTW configuration at $\mu = 0.19$.

(b) Visualisation of vorticity magnitude of distributed, OTW configuration at $\mu = 0.23$.

Fig. 22. Visualisation of vorticity magnitude of single propeller installed, and distributed OTW configurations at equivalent thrust conditions.

and horizontal propeller positioning ahead of the wing. The findings revealed that an auxiliary propeller positioned above the wing, improved the overall wing lift-to-drag ratio. This was because it decreased the stagnation area at the leading edge of the wing, and increased the velocity across the upper surface, resulting in higher suction. On the other hand, the horizontal position had minimal impact on performance.
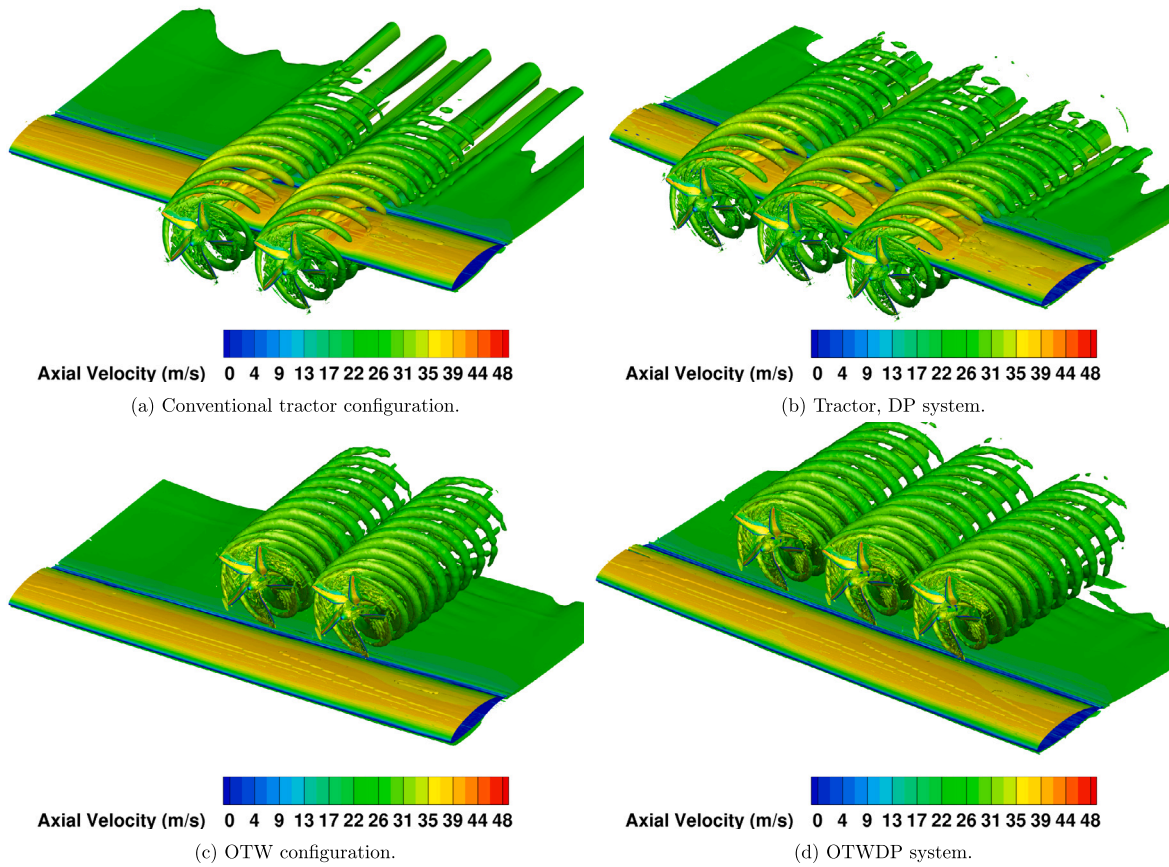
(a) Conventional tractor configuration.

(b) Tractor, DP system.

(c) OTW configuration.

(d) OTWDP system.

Fig. 23. Flow visualisation of distributed tractor and OTW configurations at $\mu = 0.42$ using iso-surfaces of Q-criteria at a value of 0.01, coloured using axial velocity.
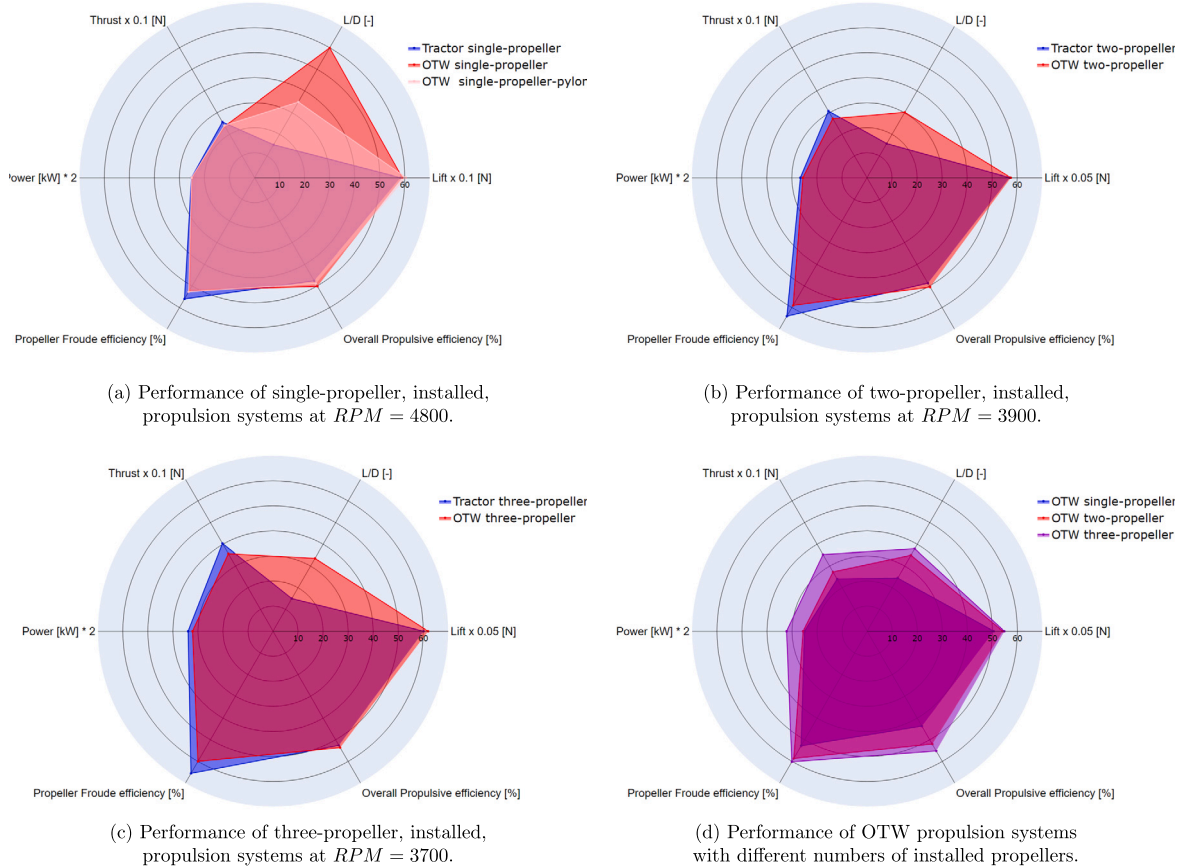

(a) Performance of single-propeller, installed, propulsion systems at $RPM = 4800$.

(b) Performance of two-propeller, installed, propulsion systems at $RPM = 3900$.

(c) Performance of three-propeller, installed, propulsion systems at $RPM = 3700$.

(d) Performance of OTW propulsion systems with different numbers of installed propellers.

Fig. 24. Comparisons of tractor and OTW configurations with single, two- and three-propeller, propulsion systems.

Using the same configuration as the X-57, the positioning of six auxiliary propellers was evaluated using Kriging at the optimisation stage. A variety of lateral and vertical positions were examined. A total of 15 sampling points were utilised, with the optimal position found above the wing, and close to the mid-chord. This position resulted in increased suction across the upper surface of the wing, with the increase extending to mid-chord. This suggests that the distributed propeller configuration enhanced the overall lift, and reduced the drag below the baseline case by shifting the propeller from the leading edge of the wing to a better position.

In the fully resolved verification section, the conformal HLP from the X-57 aircraft was utilised to assess the tractor and OTW configurations, under high-performance take-off conditions. The propeller in the OTW configuration experienced a performance drop of approximately 6.4% compared to the conventional tractor configuration. However, the optimised OTW configuration exhibited superior performance, demonstrating a 1.3% improvement in lift and a 294% increment in L/D. When considering integrated performance, the optimised OTW configuration outperformed the conventional tractor configuration by 5.5%

Additional investigations included the pylon structure effect in the OTW configuration, revealing that the pylon created more drag due to the additional surfaces. Nevertheless, the pylon retained the performance benefits in overall propulsive efficiency and lift generation. Further evaluations investigated a second propeller, demonstrating that the optimised OTW configuration led to an almost 4% improvement in overall propulsive efficiency, compared to the conventional propulsion configuration at the same lift.

In the future, the findings of this work can be used as part of an overall wing design, bringing in weight constraints and mass distribution effects due to the multiple mounted propellers.

CRediT authorship contribution statement

Geng Qiao: Writing – review & editing, Writing – original draft, Visualization, Validation, Investigation, Conceptualization. **Tao Zhang:** Writing – review & editing, Visualization, Methodology, Investigation. **George N. Barakos:** Writing – review & editing, Writing – original draft, Validation, Supervision, Investigation, Conceptualization.

Declaration of competing interest

The authors declare that they have no known competing financial interests or personal relationships that could have appeared to influence the work reported in this paper.

Data availability

Data will be made available on request.

Acknowledgements

References

[1] A. Ko, J. Schetz, W.H. Mason, Assessment of the potential advantages of distributed-propulsion for aircraft, in: XVI International Symposium on Air Breathing Engines (ISABE), 2003, pp. 1094–2003.

[2] H.D. Kim, Distributed propulsion vehicles, in: 27th International Congress of the Aeronautical Sciences, 2010, No. E-17361.

[3] H.D. Kim, J.L. Felder, M. Tong, M. Armstrong, et al., Revolutionary aeropropulsion concept for sustainable aviation: turboelectric distributed propulsion, Tech. rep., NASA Glenn Research Center, Cleveland, OH, United States, 2013, Rolls-Royce North American Technologies, Inc., Indianapolis, IN, United States.

[4] S. Clarke, M. Redifer, K. Papathakis, A. Samuel, T. Foster, X-57 power and command system design, in: 2017 IEEE Transportation Electrification Conference and Expo (ITEC), IEEE, 2017, pp. 393–400.

[5] N.K. Borer, M.D. Patterson, J.K. Viken, M.D. Moore, J. Bevirt, A.M. Stoll, A.R. Gibson, Design and performance of the NASA SCEPTOR distributed electric propulsion flight demonstrator, in: 16th AIAA Aviation Technology, Integration, and Operations Conference, 2016, p. 3920.

[6] H.D. Kim, A.T. Perry, P.J. Ansell, Progress in Distributed Electric Propulsion Vehicles and Technologies, Tech. rep., AIAA, 2020.

[7] R. De Vries, M. Brown, R. Vos, Preliminary sizing method for hybrid-electric distributed-propulsion aircraft, J. Aircr. 56 (6) (2019) 2172–2188.

[8] L. Müller, W. Heinze, D. Kožulović, M. Hepperle, R. Radespiel, Aerodynamic installation effects of an over-the-wing propeller on a high-lift configuration, J. Aircr. 51 (1) (2014) 249–258, https://doi.org/10.2514/1.C032307.

[9] E.A. Marcus, R. de Vries, A. Raju Kulkarni, L.L. Veldhuis, Aerodynamic investigation of an over-the-wing propeller for distributed propulsion, in: 2018 AIAA Aerospace Sciences Meeting, Kissimmee, Florida, 8–12, January 2018, 2018, p. 2053.

[10] R. de Vries, N. van Arnhem, F. Avallone, D. Ragni, R. Vos, G. Eitelberg, L.L. Veldhuis, Experimental investigation of over-the-wing propeller–boundary-layer interaction, AIAA J. 59 (6) (2021) 2169–2182.

[11] R. de Vries, N. van Arnhem, T. Sinnige, R. Vos, L.L. Veldhuis, Aerodynamic interaction between propellers of a distributed-propulsion system in forward flight, Aerosp. Sci. Technol. 118 (2021) 107009.

[12] R. de Vries, R. Vos, Aerodynamic performance benefits of over-the-wing distributed propulsion for hybrid-electric transport aircraft, J. Aircr. 60 (4) (2023) 1201–1218.

[13] R. Steijl, G. Barakos, K. Badcock, A framework for CFD analysis of helicopter rotors in hover and forward flight, Int. J. Numer. Methods Fluids 51 (8) (2006) 819–847, https://doi.org/10.1002/fld.1086.

[14] M. Biava, M. Woodgate, G.N. Barakos, Fully implicit discrete-adjoint methods for rotorcraft applications, AIAA J. 54 (2) (2016) 735–749, https://doi.org/10.2514/1.J054006.

[15] A. Antoniadis, D. Drikakis, B. Zhong, G. Barakos, R. Steijl, M. Biava, L. Vigevano, A. Brocklehurst, O. Boelens, M. Dietz, et al., Assessment of CFD methods against experimental flow measurements for helicopter flows, Aerosp. Sci. Technol. 19 (1) (2012) 86–100, https://doi.org/10.1016/j.ast.2011.09.003.

[16] R. Steijl, G. Barakos, CFD analysis of complete helicopter configurations–lessons learnt from the GOAHEAD project, Aerosp. Sci. Technol. 19 (1) (2012) 58–71, https://doi.org/10.1016/j.ast.2011.01.007.

[17] D. Han, V. Pastrikakis, G.N. Barakos, Helicopter flight performance improvement by dynamic blade twist, Aerosp. Sci. Technol. 58 (2016) 445–452, https://doi.org/10.1016/j.ast.2016.09.013.

[18] A.J. Garcia, G.N. Barakos, Numerical simulations on the ERICA tiltrotor, Aerosp. Sci. Technol. 64 (2017) 171–191, https://doi.org/10.2514/6.2016-0329.

[19] F. Dehaeze, G. Barakos, Mesh deformation method for rotor flows, J. Aircr. 49 (1) (2012) 82–92, https://doi.org/10.2514/1.C031251.

[20] G. Chirico, G. Barakos, N. Bown, Numerical aeroacoustic analysis of propeller designs, Aeronaut. J. 122 (1248) (2018) 283–315, https://doi.org/10.1017/aer.2017.123.

[21] C. Crozon, R. Steijl, G. Barakos, Coupled flight dynamics and CFD - demonstration for helicopters in shipborne environment, Aeronaut. J. 122 (1247) (2018) 42–82, https://doi.org/10.1017/aer.2017.112.

[22] S. Babu, G. Loupy, F. Dehaeze, G. Barakos, N. Taylor, Aeroelastic simulations of stores in weapon bays using Detached-Eddy Simulation, J. Fluids Struct. 66 (October 2016) 207–228, https://doi.org/10.1016/j.jfluidstructs.2016.07.014.

[23] G. Barakos, C. Johnson, Acoustic comparison of propellers, Int. J. Aeroacoust. 15 (6–7) (2016) 575–594, https://doi.org/10.1177/1475472X16659214.

[24] R. Higgins, A. Jimenez-Garcia, G. Barakos, N. Bown, High-fidelity computational fluid dynamics methods for the simulation of propeller stall flutter, AIAA J. 57 (12) (2019), https://doi.org/10.2514/1.J058463.

[25] R. Higgins, G. Barakos, E. Jinks, Estimation of three-dimensional aerodynamic damping using CFD, Aeronaut. J. 124 (1271) (2020), https://doi.org/10.1017/aer.2019.135.

[26] R. Higgins, A. Zarev, G. Barakos, R. Green, Numerical investigation of a two-bladed propeller inflow at yaw, J. Aircr. 57 (2) (2020), https://doi.org/10.2514/1.C035647.

[27] R. Higgins, G. Barakos, S. Shahpar, I. Tristanto, An aeroacoustic investigation of a tiltwing eVTOL concept aircraft, in: AIAA Aviation 2020 Forum, AIAA, 2020.

[28] T. Zhang, G.N. Barakos, High-fidelity CFD validation and assessment of ducted propellers for aircraft propulsion, J. Am. Helicopter Soc. 66 (1) (2021) 1–28, https://doi.org/10.4050/JAHS.66.012008.

[29] T. Zhang, G. Barakos, D. Smith, G. Barakos, A. Kusyumov, Parametric study of aerodynamic performance of equivalent ducted/un-ducted rotors, Aerosp. Sci. Technol. 117 (2021) 106984, https://doi.org/10.1016/j.ast.2021.106984.

[30] G. Qiao, Parametric study of aerodynamic performance of equivalent ducted/un-ducted propellers based on high-fidelity computational fluid dynamics, Master's thesis, University of Glasgow, 2021, http://theses.gla.ac.uk/id/eprint/82702.

[31] F.R. Menter, Two-equation eddy-viscosity turbulence models for engineering applications, AIAA J. 32 (8) (1994) 1598–1605, https://doi.org/10.2514/3.12149.

[32] G. Qiao, G.N. Barakos, Verification and optimisation of distributed propulsion using high-fidelity CFD method, in: American Helicopter Society 79th Annual Forum & Technology Display, West Palm Beach, Florida, USA, May 16–18, 2023, 2023.

[33] G. Qiao, R.J. Higgins, G.N. Barakos, T. Zhang, CFD study of eVTOL distributed propulsors, in: RAeS Applied Aerodynamics Conferencei, No. 4 Hamilton Place, London, UK, 13-15 September, 2022, https://eprints.gla.ac.uk/280193/.

[34] M. Biava, G.N. Barakos, Optimisation of ducted propellers for hybrid air vehicles using high-fidelity CFD, Aeronaut. J. 120 (1232) (2016) 1632–1657, https://doi.org/10.1017/aer.2016.78.

[35] T. Fitzgibbon, M. Woodgate, A. Jimenez-Garcia, G. Barakos, Validation of the steady-state hover formulation for accurate performance predictions, AIAA J. 57 (12) (2019) 5293–5308.

[36] H. Schlichting, K. Gersten, Boundary-Layer Theory, Springer, 2016.

[37] M. Jarkowski, M. Woodgate, G. Barakos, J. Rokicki, Towards consistent hybrid overset mesh methods for rotorcraft CFD, Int. J. Numer. Methods Fluids 74 (8) (2014) 543–576, https://doi.org/10.1002/fld.3861.

[38] R.G. Rajagopalan, S.R. Mathur, Three dimensional analysis of a rotor in forward flight, J. Am. Helicopter Soc. 38 (3) (1993) 14–25, https://doi.org/10.4050/JAHS.38.14.

[39] D.M. O'Brien Jr, Analysis of computational modeling techniques for complete rotorcraft configurations, Ph.D. thesis, Georgia Institute of Technology, 2006.

[40] T. Stokkermans, N. van Arnhem, T. Sinnige, L. Veldhuis, Validation and comparison of RANS propeller modeling methods for tip-mounted applications, AIAA J. 57 (12) (2018) 1–15, https://doi.org/10.2514/1.J057398.

[41] G. Barakos, T. Fitzgibbon, A. Kusyumov, S. Kusyumov, S. Mikhailov, CFD simulation of helicopter rotor flow based on unsteady actuator disk model, Chin. J. Aeronaut. 33 (9) (2020) 2313–2328, https://doi.org/10.1016/j.cja.2020.03.021.

[42] J. Sacks, S.B. Schiller, W.J. Welch, Designs for computer experiments, Technometrics 31 (1) (1989) 41–47, https://doi.org/10.1080/00401706.1989.10488474.

[43] P. Saves, R. Lafage, N. Bartoli, Y. Diouane, J. Bussemaker, T. Lefebvre, J.T. Hwang, J. Morlier, J.R.R.A. Martins, SMT 2.0: a surrogate modeling toolbox with a focus on hierarchical and mixed variables Gaussian processes, Adv. Eng. Softw. 188 (2024) 103571.

[44] J.R. Hooker, A. Wick, S.R. Ginn, J. Walker, B.T. Schiltgen, Overview of low speed wind tunnel testing conducted on a wingtip mounted propeller for the workshop for integrated propeller prediction, in: AIAA AVIATION 2020 FORUM, 2020, p. 2673.

[45] B.L. Litherland, N.K. Borer, N.S. Zawodny, X-57 Maxwell high-lift propeller testing and model development, in: AIAA Aviation 2021 Forum, Virtual Event, August 2–6, 2021, 2021, p. 3193.

[46] J. Yin, F. De Gregorio, K.-S. Rossignol, L. Rottmann, G. Ceglia, G. Reboul, G. Barakos, G. Qiao, M. Muth, M. Kessler, A. Visingardi, M. Barbarino, F. Petrosino, A. Zanotti, N. Oberti, L. Galimberti, G. Bernardini, C. Poggi, L. Abergo, F. Caccia, A. Guardone, C. Testa, S. Zaghi, Acoustic and aerodynamic evaluation of DLR small-scale rotor configurations within GARTEUR AG26, in: 49th European Rotorcraft Forum (ERF), Bückeburg, Germany, September 5 – 7, 2023, paper 80.

[47] B.L. Litherland, M.D. Patterson, J.M. Derlaga, N.K. Borer, A method for designing conforming folding propellers, in: 17th AIAA Aviation Technology, Integration, and Operations Conference, 2017, p. 3781.

[48] B.L. Litherland, J.M. Derlaga, A performance analysis of folding conformal propeller blade designs, in: AIAA Aviation 2019 Forum, Dallas, Texas, 17-21 June 2019, 2019, p. 3676.

[49] R.A. McDonald, J.R. Gloudemans, Open vehicle sketch pad: an open source parametric geometry and analysis tool for conceptual aircraft design, in: AIAA SCITECH 2022 Forum, San Diego, CA & Virtual, January 3-7, 2022, 2022, p. 0004.

[50] F. De Gregorio, K.-S. Rossignol, G. Ceglia, J. Yin, Multi-rotor wake interaction characterization, in: 49th European Rotorcraft Forum (ERF), Bückeburg, Germany, September 5 – 7, 2023, paper 105.

[51] J. Yin, K.-S. Rossignol, L. Rottmann, T. Schwarz, Numerical investigations on small-scale rotor configurations with validation using acoustic wind tunnel data, in: 48th European Rotorcraft Forum (ERF), 2022, 2022, pp. 1–17.

[52] J. Yin, K.-S. Rossignol, L. Rottmann, T. Schwarz, Numerical studies on small rotor configurations with validation using acoustic wind tunnel data, CEAS Aeronaut. J. (2023) 1–32.

[53] K.-S. Rossignol, J. Yin, L. Rottmann, Investigation of small-scale rotor aeroacoustic in DLR's acoustic wind tunnel Braunschweig, in: 28th AIAA/CEAS Aeroacoustics 2022 Conference, 2022, p. 2838.

[54] G. Qiao, G. Barakos, CFD validation for eVTOL propeller performance and acoustics, in: 49th European Rotorcraft Forum (ERF), Bückeburg, Germany, September 5 – 7, 2023, paper 20.

[55] Helden Aerospace, LLC., Empirical Systems Aerospace, Inc., Wind Tunnel Tesrting of Propeller Wingtip Interactions: Final wind tunnel test and CFD report for the Low Speed Wind Tunnel test of a 40.5% scale semi-span model with a wingtip-mounted propeller in the Lockheed Martin Low Speed Wind Tunnel, Tech. rep., Helden Aerospace, LLC. and Empirical Systems Aerospace, Inc., 2019.

[56] J. Sacks, S.B. Schiller, W.J. Welch, Designs for computer experiments, Technometrics 31 (1) (1989) 41–47, https://doi.org/10.1080/00401706.1989.10488474.

[57] E. Marcus, R. de Vries, A. Kulkarni, L. Veldhuis, Aerodynamic Investigation of an Over-the-Wing Propeller for Distributed Propulsion, 2018 AIAA Aerospace Sciences Meeting, American Institute of Aeronautics and Astronautics, 2018.